University of Reading

Mapping water vapour variability over a mountainous tropical island using InSAR and an atmospheric model for geodetic observations

Article

Accepted Version

Creative Commons: Attribution-Noncommercial-No Derivative Works 4.0

Webb, T. L., Wadge, G. and Pascal, K. (2020) Mapping water vapour variability over a mountainous tropical island using InSAR and an atmospheric model for geodetic observations. Remote Sensing of Environment, 237. 111560. ISSN 0034-4257 doi: 10.1016/j.rse.2019.111560 Available at https://centaur.reading.ac.uk/87723/

It is advisable to refer to the publisher's version if you intend to cite from the work. See Guidance on citing.

To link to this article DOI: http://dx.doi.org/10.1016/j.rse.2019.111560

Publisher: Elsevier

All outputs in CentAUR are protected by Intellectual Property Rights law, including copyright law. Copyright and IPR is retained by the creators or other copyright holders. Terms and conditions for use of this material are defined in the End User Agreement.

University of Reading

www.reading.ac.uk/centaur

CentAUR

Central Archive at the University of Reading

Reading's research outputs online

Mapping water vapour variability over a mountainous tropical island using InSAR and an atmospheric model for geodetic observations

T. L. Webb[1,2], G. Wadge[1], K. Pascal[3,4]

1. Department of Meteorology, University of Reading, UK
2. Laboratoire d'Aérologie, Observatoire Midi-Pyrénées, Toulouse, France
3. Montserrat Volcano Observatory, Montserrat
4. Seismic Research Centre, University of the West Indies, Trinidad & Tobago

Abstract

The three dimensional distribution of water vapour around mountainous terrain can be highly variable. This variability can in turn affect local meteorological processes and geodetic techniques to measure ground surface motion. We demonstrate this general problem with the specific issues of a small tropical island, Montserrat. Over a period of 17 days in December 2014 we made observations using InSAR and GPS techniques, together with concurrent atmospheric models using the WRF code. Comparative studies of water vapour distribution and its effect on refractivity were made at high spatial resolution (300 m) over short distances (~ 10 km). Our results show that model simulations of the observed differences in water vapour distribution using WRF is insufficiently accurate. We suggest that better use could be made of the knowledge and observations of local water vapour conditions at different scales, specifically the Inter Tropical Convergence Zone (ITCZ), the trade wind fields and the mountain flow (~30

m) perhaps using eddy simulation. The annual perturbations of the ITCZ show that the range of humidity is approximately the same expressed as the differential phase of InSAR imaging (~100 mm). Trade wind direction and speed are particularly important at high wind speeds driving vigorous asymmetrical convection over the island's mountains. We also show that the slant angles of radar can follow distinct separate paths through the water vapour field. Our study is novel in demonstrating how synoptic-scale features and climate can advise the modelling of mesoscale systems and sub-seasonal InSAR imaging on tropical islands.

Keywords: water vapour, mountainous tropical island, ITCZ, InSAR

1. Introduction

Variation in the refractivity of the Earth's atmosphere can change the path and travel time of radiation passing through it. Making use of this behaviour contributes to boundary-layer meteorology (Stull, 1988), geodetic techniques such as Global Navigation Satellite Systems GNNS (Hofmann-Wellenhof et al., 1995) and synthetic aperture radar interferometry (InSAR) (Hanssen, 2001). Changes in refractivity are characterised by air temperature and pressure, particularly the partial pressure of water vapour (Bevis et al., 1994). Water vapour content generally increases downwards through the atmosphere and is most variable within the atmospheric boundary layer (ABL), a few kilometres thick and is the dominant reservoir of water vapour (Bengtsson, 2010).

Here we are mainly concerned with the varying refractivity of the atmosphere as it affects data collected by the InSAR method in which two phase images of the scene of interest are acquired at different times, but from very similar orbital positions, yielding coherent images of differential phase "delay". A common goal is to acquire the differential phase corresponding to land surface motion, having systematically removed or minimised the other "noise" effects (Hanssen, 2001). Of these effects, atmospheric water vapour variability has been the most difficult to remove. This is because of its rapid decorrelation over length scales of ~ 100s of km and time scales of ~ 10s of days that are typical of Low Earth Orbit (LEO) radars used for most InSAR missions. Ways to mitigate the atmospheric noise have included independent observations of water vapour (e.g. GNSS, Li et al., 2005); the use of statistical time series methods with long datasets (e.g. Bekaert et al., 2015; Li et al., 2019) and models that simulate the atmosphere at the time of radar imaging. (e.g. Jolivet et al., 2011, 2014). The latter is the approach we use here, which is of considerable generality but difficult to apply in practice. For example, the initial conditions for the model are hard to generate, and convection is difficult to represent without using parameterizations. We do present other relevant data (e.g. GNSS and radiosonde), but do not attempt to combine them with atmospheric modelling to find an optimal joint solution. Montserrat is fortunate in having a dense network of GPS stations and a radiosonde site at a distance of ~100 km. We use these two sources to generate water vapour variability measurements to validate the numerical model- radar approach.

Conventionally for InSAR, the atmospheric contribution to the radar delay is considered to comprise four major components: Wet Delay (WD, due to water vapour), Liquid Water Delay (LWD), Hydrostatic Delay (HSD, due to atmospheric pressure) and Ionospheric Delay (due to electron density in the area of the atmosphere affected by solar radiation), (Hanssen, 2001). Recent studies (Feng et al., 2017) ; Fattahi et al., 2017), have shown that the ionospheric contribution can be significant for low frequency radars (e.g. L-band, 1.27 GHz) studying large length scales (several 100 km). For our scale of study, the magnitude of ionospheric phase delay at a much higher frequency (X-band, 9.65 GHz) and a much smaller length scale (~10 km), are of much lower magnitude, allowing us to ignore that component. Hydrostatic delay variation can be significant at times of large surface pressure change (Tregoning and Herring, 2006), in areas of great topographic relief (~ 5 km, Elliott et al, 2008). We choose to ignore this effect in the case of Montserrat.

Differential InSAR, in which phase difference images are created from pairs of radar images separated in time, is sensitive to the changes in liquid water in clouds and particularly water vapour content along the radar path over this time period. Differential InSAR is an increasingly valuable tool for monitoring volcanoes (e.g. Lu and Dzurisin, 2014). Differential ground motions of a few mm can be detected and modelled in terms of pressurized magma storage and eruption processes (Pritchard et al., 2018; Ebmeier et al., 2018). However, many volcanoes have substantial edifices (>1 km high) such that the radar path to the base of the volcano has to pass through more water vapour than the equivalent path to the summit of the volcano. In this way the phase difference can be strongly modulated by topography. The resulting pattern of phase differences may be very similar to surface deformation generated by a pressure source centred within or below the edifice. This potential confusion of signals has been the subject of considerable study (e.g. Massonnet and Feigl, 1998; Wadge et al., 2002). This is particularly relevant for volcanoes that have high relief and which generate complex patterns of airflow associated with that relief. In these cases it is not just the topography that modulates the water vapour field but the dynamic flow of air over and around it. Here we address these processes using repeated InSAR measurements and numerical models of the delay due to atmospheric water vapour content.

The physical and temporal scales of the radar results and the steep island terrain provides a set of constraints distinct from equivalent continental scale studies (~10^5 – 10^4 km^2), that tend to rely on the analysis of large radar datasets (e.g. Bekaert, et al., 2015, Alshawaf, et al., 2015). This in turn gives us the opportunity to better understand small-scale (~10^3 – 10^2 km^2) processes involving the distribution of water vapour. Our investigation is set in the humid tropics. This has a distinctive climate driven by the Inter Tropical Convergence Zone (ITCZ) (Schneider et al., 2014), the Low-Level Jet (Munoz et al., 2008) and their interrelationship (Laderach and Raible, 2013) It is this combination of tropical climatology, diurnal boundary layer dynamics and localised, steep topography that is clearly important but little studied and forms the innovative basis of our study. Rather than relying on ever more difficult-to – constrain initial conditions to the simulation of local delay fields, we propose that bringing to bear climatological data and insights will enable improved models to be created .We demonstrate this approach qualitatively in Fig. 1.

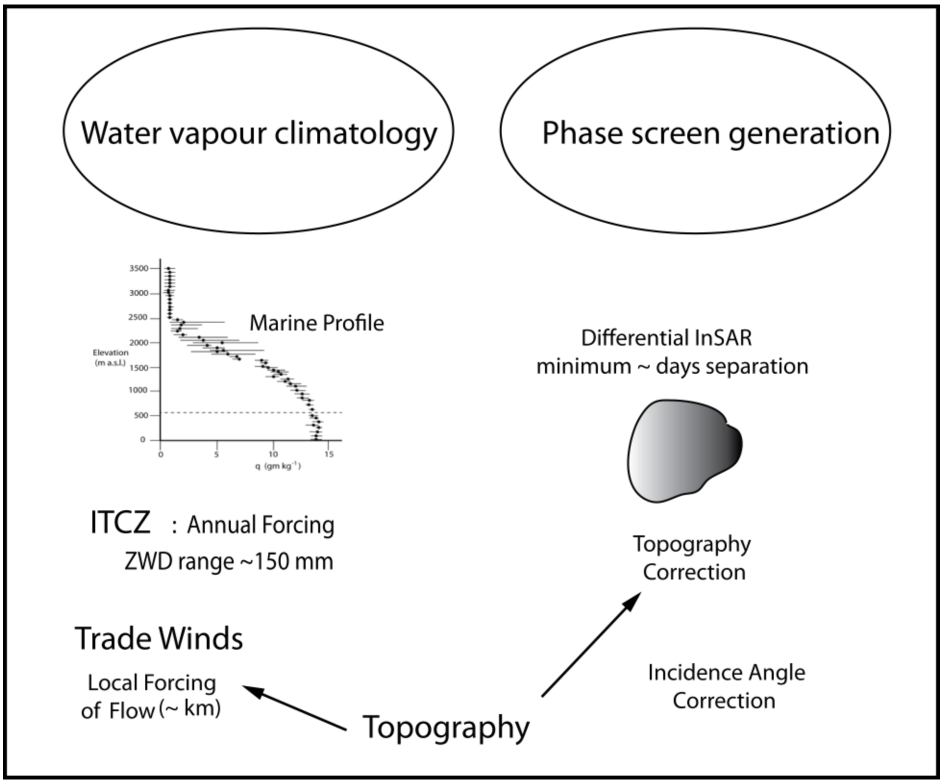

Fig.1 Schematic illustration of the potential use of water vapour climatology to mitigate the effects of tropospheric phase delay water vapour variability. On the right is a set of standard processing measures in the use of differential InSAR, as used in this study. In contrast, on the left are three aspects of water vapour climatology discussed in the text. Note that, apart from topography, there is no treatment that links the two sets of measurements.

The objectives of this study are to:

1.1 Understand where and when tropical water vapour originates.

1.2 Measure and simulate the water vapour field over a small mountainous tropical volcano using InSAR phase fields, equivalent atmospheric models and GNSS (and local field data) during a 17-day campaign.

1.3 Show that the ambient state of the ITCZ, the trade winds and the radar viewing geometry can play important roles in the variability of water vapour.

These objectives provide the structural sub-headings used in the Discussion.

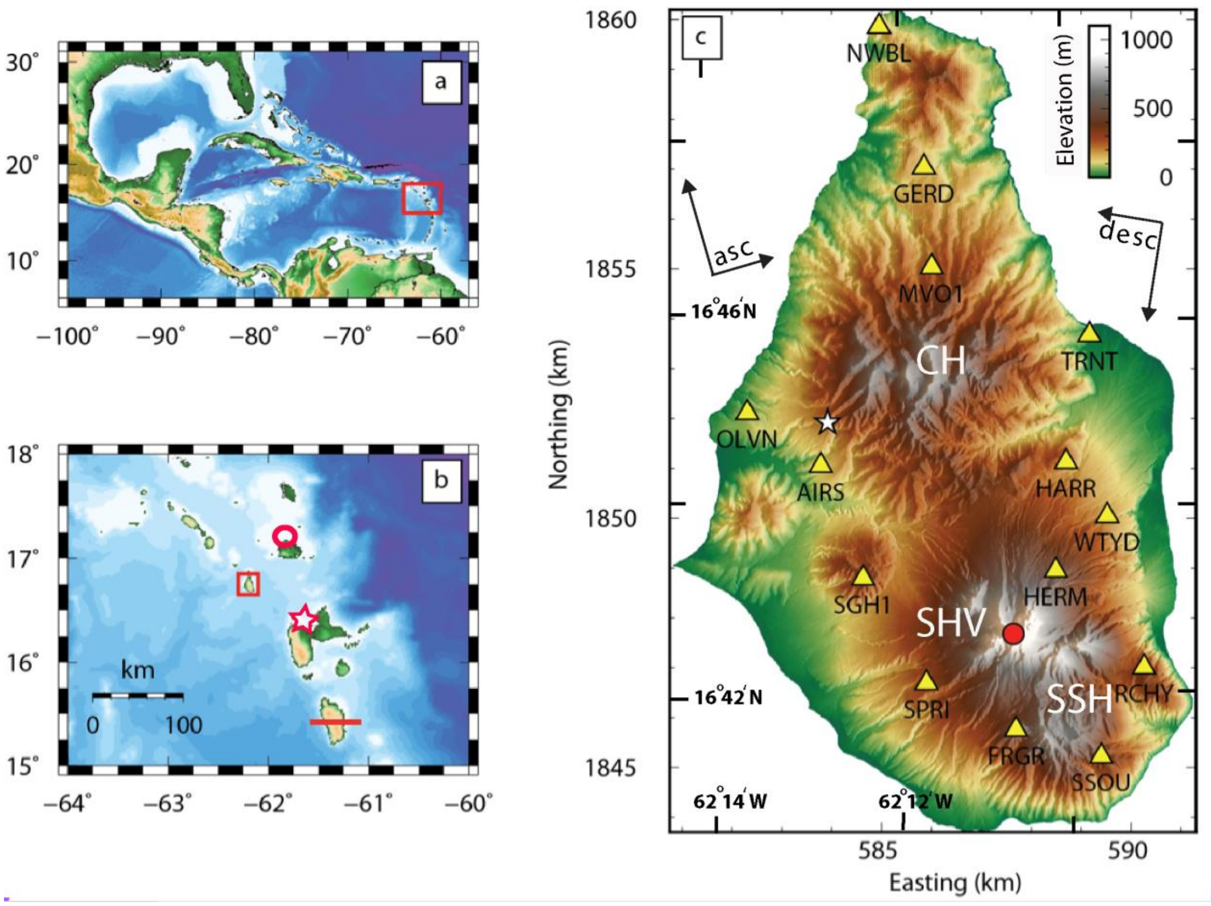

Fig.2 Location of Montserrat. (a) In the eastern Caribbean Sea (red box) , (b) In the central Lesser Antilles, framed by a red box. The red circle denotes the location of Antigua (Fig.4), the red star represents Le Raiset, Guadeloupe where sondes are launched (Fig. 12), and the red line represents the transect across Dominica for the model results shown in Fig.8).(c) Shaded elevation map of Montserrat (McVicar and Korner, 2013) showing the locations and names of the continuous GPS stations (yellow triangles). The white star gives the position of the Montserrat Volcano Observatory and the red circle is the lava dome of the Soufrière Hills Volcano (SHV). CH is the location of the Centre Hills, SSH is the South Soufrière Hills. ASC shows the orientation of the ascending pass satellite track and incidence azimuth. DESC shows the same for the descending pass satellite track. The internal coordinates are latitude and longitude, the external coordinates are the local grid for Montserrat.

2. The Study Site: Montserrat, Lesser Antilles

We base our study on Montserrat (Fig. 2), a small (~10 x 16 km) volcanic island in the Lesser Antilles (17°N, 62°W). The Soufrière Hills Volcano (SHV), whose summit is about 1083 m above sea level (a.s.l), occupies the southern half of the island, and has been active since 1995, causing the destruction of the capital city Plymouth and the emigration of more than half the population (Fig.2c) (Wadge et al., 2014). Improved geodetic monitoring is important for the mitigation of future volcanic risk in Montserrat (Odbert et al., 2014) and at other similar volcanoes.

The Lesser Antilles islands sit in the eastern Caribbean Sea a region of atmospheric interactions that determine the humidity, winds and rainfall experienced (Taylor and Alfaro, 2005). The main mechanisms involve the Atlantic, or western, part of the Inter Tropical Convergence Zone (ITCZ) and the North Atlantic Subtropical High (NASH) (Waliser and Gautier, 1993; Martinez et al., 2019). The ITCZ is a global zone of clouds and storms together with the trade winds blowing from the east and from the east southeast at different times of year (Richter et al., 2017). The NASH provides strongly divergent winds and atmospheric subsidence in the eastern Caribbean atmosphere. As the ITCZ migrates northwards away from the equator in the boreal summer, it reaches its most northerly position in June, July and August (JJA). Specific humidity increases at the latitude of Montserrat, within a range of about 1- 6 g/kg (Fig.3). However, this field is highly smoothed in Fig.3 and humidity varies strongly on a small scale in both space and time (Bengtsson, 2010).

The ITCZ is particularly important because the evaporation flanking the ITCZ forms the main baseline source of humidity for the Lesser Antilles. Figure 3 shows the zonal mean distribution of observed specific humidity and precipitation based on ERA-interim reanalysis data (Laderach and Raible, 2013) for July, the pivotal point of the migration. The ITCZ migration from the equator during JJA also involves the strengthening of the southeast trade winds at ground level, from 3.2 m/s in April to 5.4 m/s in July (Richter et al., 2017).

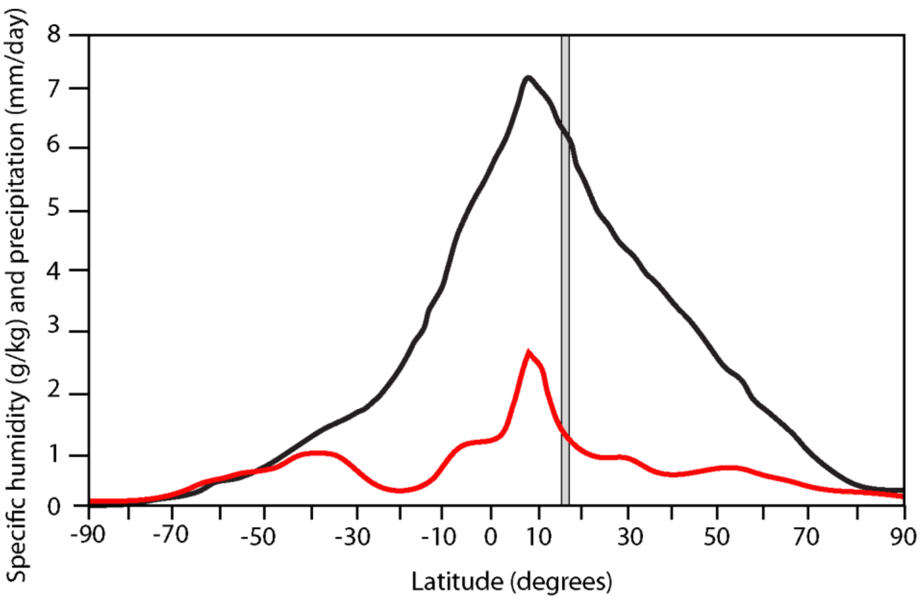

Fig.3 Latitudinal plot of the zonal mean distribution of observed specific humidity and precipitation of the ITCZ for July from 1979 to 2010. The black curve is from ERA-interim specific humidity data, the red curve is for precipitation. The grey rectangle covers the location of the study site (after Laderach and Raible, 2013).

Figure 4 shows the annual impact that the ITCZ has on rainfall in the Lesser Antilles, in this case in Antigua, to the northeast of Montserrat (Fig.2b). December to March is a dry season followed by rising rates of rain with an irregular peak in November, a pattern common to many islands in the Lesser Antilles. The difference in rainfall rate over the year due to the migration of the ITCZ in the Eastern Caribbean is about 5 mm/day (Fig.4).

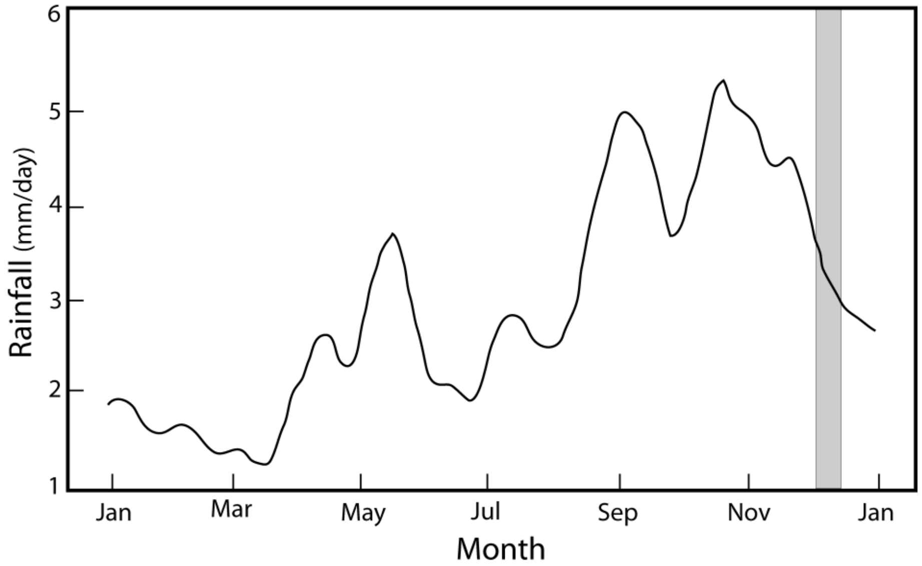

Fig.4 Rainfall climatology for 1969-2017 at Antigua, northeast of Montserrat. Values are average rainfall in mm/day (adapted from Martinez et al., 2019). The grey band is the period of radar data acquisition in December 2014 that is studied in detail.

Another significant feature of the tropical circulation are the low level jets (LLJs). These are regions of high winds in the lower troposphere coupled with an annual cycle of precipitation and a rainy season extending from May through October in the Caribbean (Munoz et al., 2008). There is a temporal maximum in wind speeds in July and a minimum in February (Fig.5). Spatial (zonal) wind speed maxima occur at a pressure of about 925 hPa (~700 m above sea level) with speeds reaching maxima of ~ 14 ms^{-1} in July and minima of ~8 ms^{-1} in October (Fig.5). Diurnal wind speed variability tends to peak in the morning.

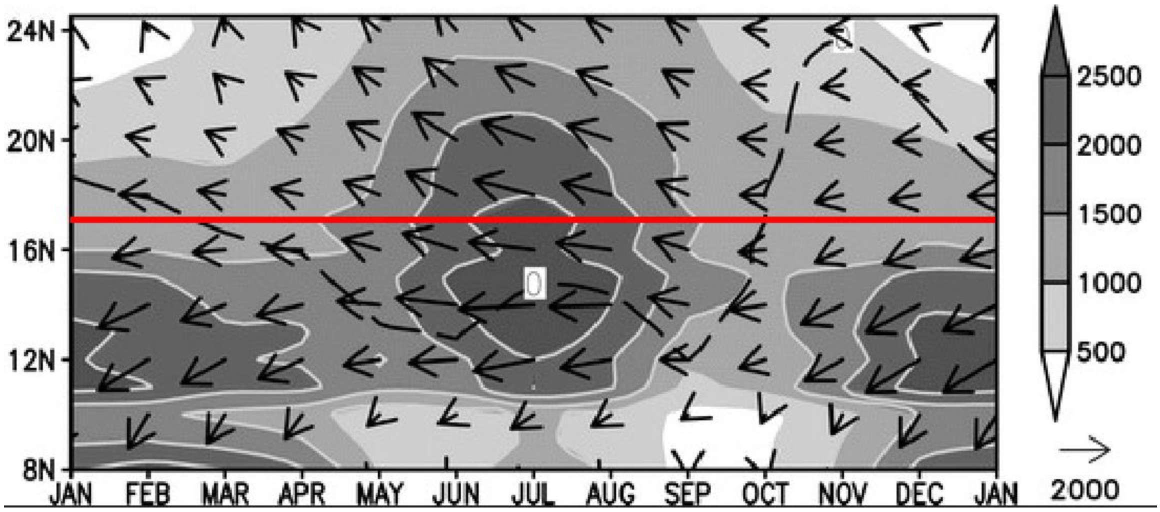

Fig. 5 The zonal moisture flux across the Caribbean plotted in latitudinal-monthly space. The grey shading is of moisture flux and the arrows are moisture flux vectors generated from the North American Regional Reanalysis (NARR, Munoz et al., 2006). Montserrat's location is represented by 17N latitude (solid red line)and by December.. The moisture flux decreases about a peak value in July of 2500 g kg^{-1} m s^{-1} to about half that between October and April.

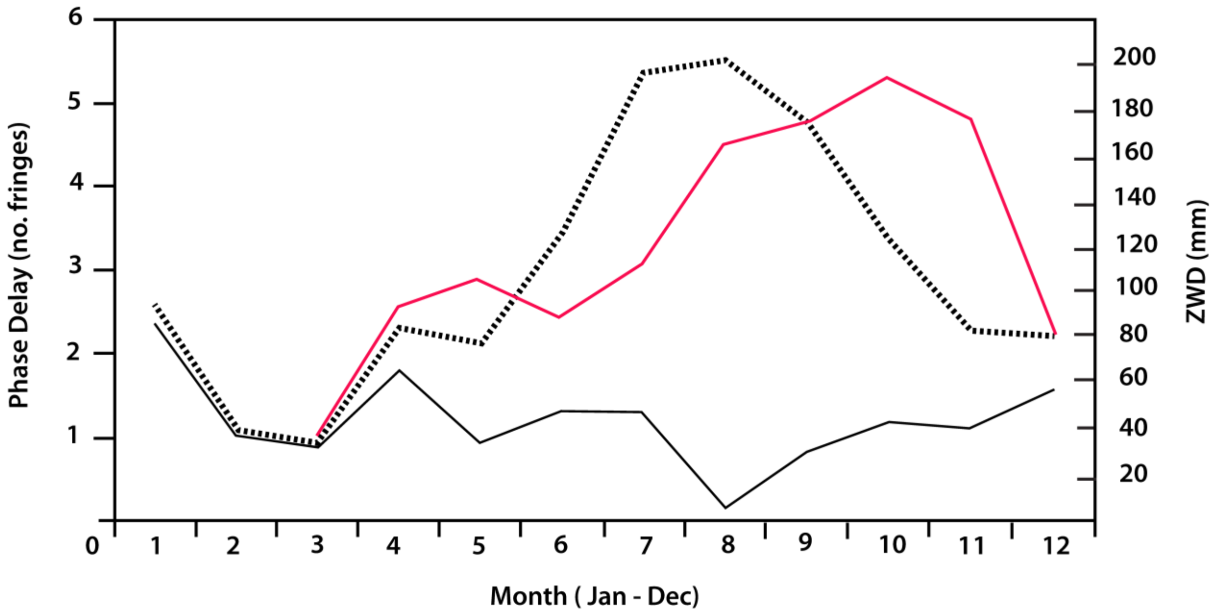

Fig.6 Plot of monthly mean phase delays at Fogo volcano between June 2005 and December 2007 (Black dashed line gives the number of delay fringes, black continuous line gives the standard deviation) (adapted from Heleno et al., 2010). Red line gives an equivalent plot of monthly phase ZWD delays averaged from March 1998 to November 2000 at SHV volcano on Montserrat (taken from Wadge et al., 2006).

In the eastern Atlantic part of the ITCZ, the Fogo Volcano shows a similar behaviour to that at SHV, Montserrat (Heleno et al., 2010). Using a 2.5 year-long dataset of 71 ASAR radar images Heleno et al. were able to show strong seasonal signals of humidity and resulting phase delay (Fig.6). The amplitude of the ITCZ-derived annual variability of water vapour at Fogo was measured at up to 17 cm of equivalent ground motion between sea level and about 2000 m a.s.l. (Fig.6). This agrees with independent MODIS-derived, precipitable water vapour (PWV) values. Montserrat has a similar annual relationship to Fogo in this regard. Fig.6 shows the monthly ZWD variation values over a 2.5-year period. Whilst the SHV and Fogo have slightly different peaks in their water vapour contents the broad pattern of dominant water vapour content in the winter is obvious. Effectively, much of the seasonal water vapour signal variability is generated by the ITCZ migration. From the perspective of InSAR geodetic monitoring, the variability of differential phase will tend to be much greater if the interferometric pair comprises data from, say, May and November, rather than from January to April (Fig.6).

The strength and timing of the ITCZ varies from season to season and from one year to the next. For example, the wind direction data collected by Wadge et al., (2006) on Montserrat between 1998 and 2000 (Table 5) shows monotonous easterly winds in April and highly variable winds in July.

In addition to the ITCZ, weather systems at the 100-1000 km scale affect Montserrat. These include cyclonic systems, up to hurricane strength, carried westward across the Atlantic as “easterly waves” during the wet season, together with locally originating large convective systems (Matthews et al., 2002; Barclay et al., 2006). Troughs of dry upper tropospheric air also occur in the eastern Caribbean (e.g. Wadge et al., 2016). From our perspective the most significant impact that these events have is their disruption of the ABL, particularly the speed and direction of the wind over the island.

The ABL over the sea surrounding Montserrat is relatively simple compared to that over the islands. The Atlantic Ocean ABL upwind from Montserrat was studied by the Barbados Oceanographic Meteorological Experiment (BOMEX), (Siebsma et al., 2003) and the Rain in Cumulus Over the Ocean (RICO), (Davison et al., 2013) field measurement campaigns. Typically, cumulus cloud develops over the sea during the day, usually below a temperature inversion. These clouds and other sub-cloud, high-moisture content air parcels act as triggers for buoyant convection when advected over land (Kirshbaum and Smith, 2009) resulting in taller and broader cumulus clouds over the islands. The water vapour field over the open ocean, measured in the RICO study, typically takes the form of the profile shown in Fig.7 (Stevens, 2006). Below the lifting condensation level (LCL) the water vapour specific humidity is fairly constant and reaches the highest values. Above it, within the cloud layer, the mean specific humidity decreases strongly with altitude but its variability increases (Fig.7). Above the cumulus layer the humidity often has a low, uniform value. Typically, the ABL has a thickness of about 2 km but it can be up to 4 km in the winter months (Davison et al., 2013). Radiosonde-derived specific humidity profiles for the days of radar imaging are discussed in section 5.1. A strong diurnal cycle of water vapour variability was observed on 4-5 August, 2013 in the ground radar interferometer measurements of Wadge et al. (2016) over Montserrat. The windward slopes of the mountains were heated first at sunrise and a rapidly mixing layer driven by convective heating developed over about 2 hours. This reached its maximum development in the early afternoon. After sunset the ABL rapidly evolved to a much weaker mixed layer above a lowermost stable layer, with greatly reduced variance in water vapour.

The trade winds in the Lesser Antilles mainly blow from east northeast. The relatively uniform marine ABL changes its structure due to the interaction with topography and the daytime heating of the islands' surfaces. The trade winds blow roughly perpendicular to the topographic axes of the islands in the northern and central part of the arc such as at Montserrat, giving asymmetrical windward and leeward characteristics. The speed and direction of the trade winds play important roles in the development of clouds, precipitation and topographic flows. The atmospheric processes over some of the islands of the Lesser Antilles have been studied intensively in recent years. These include: cloud trails forming due

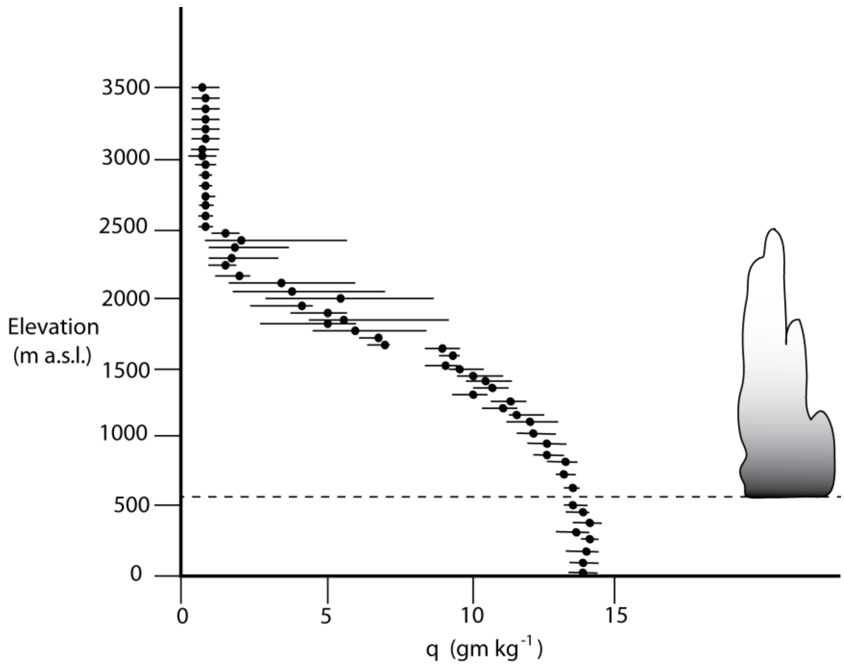

Fig.7 Profile of water vapour specific humidity (q) values measured during the 10th research flight of the RICO campaign (Stevens, 2006). Above the LCL (dashed line, ~600 m a.s.l.) mean values of q (black dots) decrease up to the top of the cumulus layer at about 2200 m a.s.l. (shown schematically on the right), whilst the variability increases (black lines are the interquartile ranges).

to diurnal heating (Smith et al., 1997; Kirshbaum and Fairman, 2015), island-induced winds, including katabatic flow (Cécé et al., 2014), orographic precipitation (Kirshbaum and Durran, 2004; Kirshbaum and Smith, 2009; Smith et al., 2012), orographic convection (Minder et al., 2013; Nugent et al., 2014; Wang and Kirshbaum, 2015) and volcanically-triggered rainfall (Poulidis et al., 2016).

Dominica (200 km to the southeast of Montserrat) experiences similar trade wind weather to Montserrat, and as shown in Fig.8a. For low wind speeds (<5 m/s) diurnal thermal convection dominates (Smith et al., 2012), and the eastern (windward) side of the island in the case of low wind speeds from the north, the eastern side of the island has a much more complex humidity field than the western (lee)side. For high wind speeds (>7 m/s, Fig.8b) mechanically driven convection occurs, most strongly over the eastern windward slopes, and the form of the resultant water vapour field is reversed, with drier air above the leeward slopes. On Dominica, Minder et al. (2013) showed that at high wind speeds (~12 m/s), plunging flow on the leeward (western) slopes of the mountain reduces the specific humidity, at altitudes below about 1-1.5 km a.s.l. and around the summit, by up to 3-4 g/kg relative to values on the windward (eastern) side.

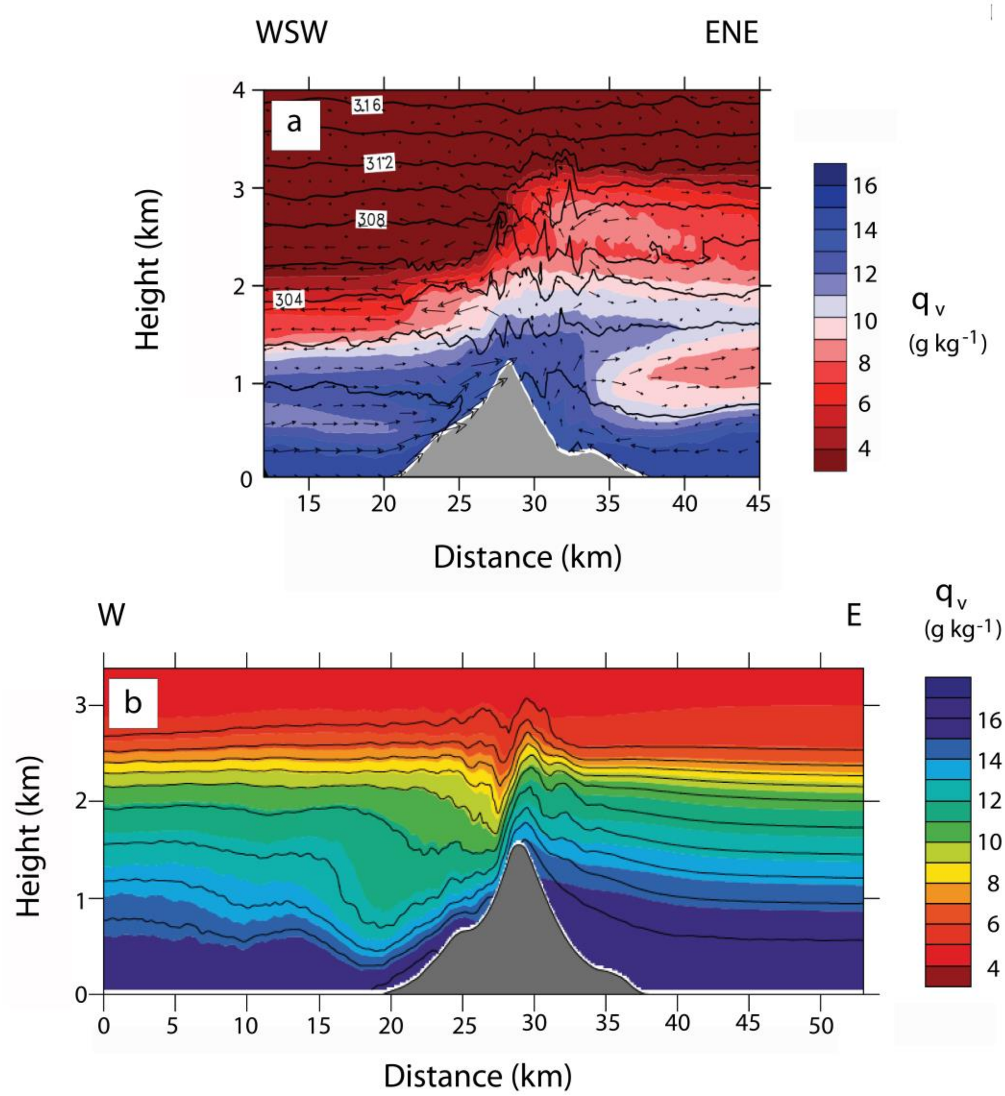

Fig.8 Transects of modelled specific humidity fields from Dominica whose locations are approximately shown in Fig.2b. (a) Low wind speed WRF model with an ENE-WSW section output of a 4-hr averaged water vapour specific humidity field (q_v, coloured) over Dominica. The wind direction is shown by arrows and the speed is low, about 2 m/s, from the north. Potential temperatures are given by the black lines. Data courtesy of D. Kirshbaum, from the study of Wang and Kirshbaum (2015). (b) High wind speed WRF model with an E-W section output of 6-hr averaged water vapour specific humidity field (coloured) over Dominica. The trade winds blow from the right (east-south-east) at a speed of about 12 m/s (from Minder et al., 2013).

Sometimes a train of lee waves will develop. Figure 9a shows an example of this captured by MODIS imagery of Montserrat at 17:30 local time on 3rd August 2013. A WMM image of integrated water vapour content for the same time (Fig.9b) simulates well the two strong waves that developed to the lee side of the island. The lee waves have peak-to-trough amplitudes of about 15 mm of ZWD.

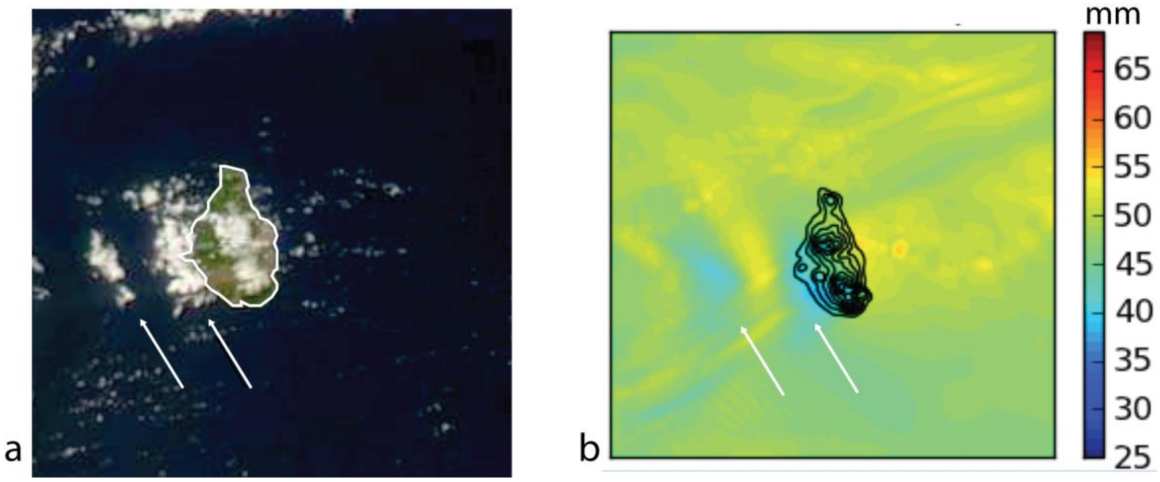

Fig. 9 Lee waves produced downwind of Montserrat during trade wind flow at 17:30 on 3rd August 2013. (a) MODIS Terra image showing Montserrat (16 km N-S), outlined in white, covered in green vegetation and buff volcanic deposits. Three banks of cumulus cloud produced by lee waves (white arrows) are evident. (b) WMM simulation, at same time as (a), of the vertically integrated water vapour content. See Fig.S1 for GPS-ZWD calculation.

3. Methods

3.1 InSAR

A radar image of the ground surface, when compared to a geometrically equivalent image acquired at another time can give a coherent measure of the phase change during that interval. This is the principle of InSAR and, as in our case, the interferograms are acquired every few days by radar-hosting satellites in sun-synchronous dawn-dusk orbits (Hanssen, 2011), using GAMMA software. We requested from the Italian Space Agency (ASI) an intensive observation campaign using the COSMO-SkyMed constellation of four X-band radars between

2 and 19 December 2014 (2,3,6,10,14,18,19 December). We made meteorological observations on the ground in Montserrat during the satellite imaging. The measured phase in the interferograms is the combined sum of components derived from the orbit (Fattahi and Amelung, 2014), the viewing geometry (Goldstein and Werner, 1998), the topography (Spaans and Hooper, 2016), the motion of the ground, the refractive delay of the atmosphere (Li et al., 2019), the nature of the surface scattering and noise (Zebker and Villasenor, 1992). In our case we can explicitly correct for the geometry from knowledge of the satellites' orbits and for the topography by using a 25m-DEM. GPS measurements made by MVO, show that there was no significant ground deformation during our survey (Stinton et al., 2016). The residual signal should be that due to the change in refractivity and noise, including uncompensated ground surface change.

Table 1. COSMO-SkyMed imaging times and angles

Date	Pass	Image Time (local time)[3]	Sunrise/Sunset (local time)	Incidence Angle[1] (°)	Azimuth Angle[2] (°)
2/Dec/2014	asc	05:58	06:20	26.6	069
3/Dec/2014	asc	05:58	06:21	26.6	069
6/Dec/2014	des	17:34	17.35	59.2	281
10/Dec/2014	des	17:34	17:37	59.2	281
14/Dec/2014	des	17:34	17:38	59.2	281
18/Dec1/2014	asc	05:58	06:29	26.6	069
19/Dec/2014	asc	05:58	06:30	26.6	069

1. Angle from vertical of radar impinging on surface.
2. Direction of look of radar in the horizontal plane (0-360° N=0, clockwise).
3. Local time is UTC - 4 hr.

Table 2. Meteorological conditions at radar overpass

Date	T (°C)	RH (%)	WV Lapse Mm/m	Wind RS[1] (°) /m/s	Wind G[2] (°) /m/s	Wind TR[3] (°) /m/s
2/Dec/2014	24	89	0.075	087/5	070/2	175/1
3/Dec/2014	24	89	0.107	040/3	030/11	140/2
6/Dec/2014[4]	23	90	0.097	258/5	330/7	190/2
10/Dec/2014[5]	25	80	0.098	148/6	170/3	100/2
14/Dec/2014	25	70	0.098	135/9	170/3	100/2
18/Dec/2014	23	83	0.095	009/1	070/2	000/2
19/Dec/2014	24	78	0.083	084/10	110/6	-

T = temperature, RH = relative humidity, WV lapse = water vapour content lapse rate

1. Wind velocity measured by radiosonde above Guadeloupe (<600m asl).
2. Wind velocity measured by anemometer at Geralds airport.
3. Wind velocity measured at Tar River GPS site.
4. Mesoscale cumulus to southeast.
5. Cloud trails SSE to NNW (Kirshbaum and Fairman, 2015).

Table 1 gives details of the radar image acquisitions and table 2 gives the meteorological conditions at the times of acquisition.

Random changes in time in the location or strength of the local scatterers within a radar beam will increase the phase noise. Surfaces covered by wind-blown trees or rapidly growing vegetation can become incoherent, whilst the phase signal from a rocky or soil-covered surface may remain coherent. On Montserrat, the forests (at South Soufrière Hills and Centre Hills, Fig.2c) become incoherent to X-band radar signals over a few hours. Because the phase gathered by InSAR systems is modulo 2pi, the ambiguity this creates must be removed by unwrapping of the phase signal. Here we use a minimum cost flow method (Costantini, 1998). Areas with incoherent signal or poor unwrapping of phase are masked. The ascending and descending pass masks are different in detail, reflecting their viewing geometries, but largely comprise the areas of Centre Hills and South Soufriere Hills (Fig.2c), which were not denuded of forest cover during the 1995 - 2010 eruption.

3.2 Atmospheric Models

The small size of Montserrat requires a high-resolution model to represent both the topography and its impact on airflow over and around it. The model used is the WRF Montserrat Model (WMM) and a detailed description of the WMM can be found in Webb (2015). Céce et al., (2014) used a similar, though coarser, WRF-based model to represent Guadeloupe. The WMM uses the European Centre for Medium-range Weather Forecasting, (ECMWF) operational forecast data on a 16 km grid truncated onto a horizontal 19 km grid level as its initial condition, and simulations are successively nested through domains with 8.1 km, 2.7 km, 0.9 km and 0.3 km grids. The lower domain boundary is a 30 s regional terrain dataset imposed on all nested grids, except the 0.3 km grid, whose surface is represented by a bespoke mapping of the cover of Montserrat by water, farmland, forest and bare rock. The topography is represented by a 25 m horizontal resolution DEM. Table 3 shows the parameterizations used in the WMM at each domain level. In the vertical, the grid comprised 51 eta levels (using a terrain-following hydrostatic pressure coordinate) skewed to the lower troposphere – the lowest region of the atmosphere. A few closely packed layers near the upper domain boundary (20 km) were used to control wave reflections. Adaptive time stepping was used (see table 3) and controlled by the stability of the Courant-Friedrichs-Lewy condition on the innermost domain. The model spin-up time was 10 hours.

Table 3. Parameterisation options for WMM in each spatial domain

	Domain 1	Domain 2	Domain 3	Domain 4
Resolution (km)	8.1	2.7	0.9	0.3
Starting Ts^{-1}	10	8	6	4
i start offset[2]	1	65	65	52
j start offset[3]	1	65	62	62
Cumulus	Grell Devenyi	Grell Devenyi	None[4]	None[4]

For each of the following parameters the values are common to all domains: Grid size (km), vertical levels (50, Planetary Boundary Layer = Yonsei, Radiation = Dudhia RRTM, Microphysics = Ferrier, Cumulus physics calls (min.) = 8, PBL physics calls = 8.

[1]Timestep used at start of a model run before adaptation by the CFL condition.

[2]Grid offset from previous domain, units determined by outer domain.

[3]No cumulus parameterisation needed at this domain resolution.

[4]A call time of 0 means at every time-step.

From the WMM results we calculate the two-way travel zenith path delays for each day of the 2,3,6,10,14,18,19 December dataset. We also differenced (earlier-later) the pairs of slant wet delay (SWD) fields from the WMM models corresponding to COSMO-SkyMed interferograms and then subtracted the WMM SWD fields from the interferograms. Identical fields would, assuming no other processes introducing signals, result in a perfect compensation for the observed water vapour delay and leave a uniform phase field.

3.3 GPS

MVO operates a network of 14 continuous GPS stations across Montserrat (Fig.2c). The data are telemetered to MVO and processed using GAMIT/GLOBK software (Herring et al, 2010 a, b). At any given interval there is a varying subset of the full GPS satellite constellation visible to each GPS site. The angle of elevation above the horizon of each satellite is variable. A threshold elevation angle of 10° was used to reduce the noise from low-angled paths (Fig.10). The refractive delay of the signal is greater for a satellite-GPS station path with a low elevation angle. An estimate of the Zenith Total Delay (ZTD) (Herring et al., 2010) , was made using the GAMIT/GLOBK processing suite incorporate the GPT2 model (Lager et al., 2013), which combines the Global Pressure and Temperature (GPT) and Global Mapping Function (GMF) empirical models, increasing their spatial (5° vs 20° grid) and temporal resolutions (annual and semi-annual vs annual variations only), and provides daily a priori values of pressure, temperature, water vapor pressures, and mapping function coefficients with a sampling rate of 30 s corresponding to the GNSS observations sampling rate. To further improve the accuracy of the a priori temperature and pressure values at each GNSS stations, specifically at the time of InSAR image acquisition (5h58 and 17h34 East Caribbean Time), we extract them from the global climatic model NCEP. A comparison of the ZHD values computed using temperatures and pressures from the GPT2 and the NCEF model shows an improvement of up to ~ 100 mm. The ZWD (in mm of phase delay) equivalence to the water vapour amount (in mm of precipitable water) is about 7 mm of phase delay to 1 mm of water. The values of ZWD are calculated every hour using a piecewise linear function.

The accuracy of the ZWD estimate depends on the location of the satellites. The measurement space for each GPS site is an inverted cone (Fig.10a). The GPS stations are well distributed across the island, with nearest neighbour spacing of ~3 km (Fig. 2c). Stations on or near the coast will have substantial parts of their measurement space over the sea. Depending on the paths, this could lower the variability of the estimates if the marine troposphere is more uniform than the island troposphere.

The elevation range of the GPS network covers only about half the vertical range of the island's topography (12 to 589 m a.s.l. compared to 0 to 1083 m a.s.l.). Steep topography may cause the line of sight of GPS to become blocked (Fig.10). With increasing elevation of the GPS site, the measured ZWD value will tend to fall. The lapse rate of ZWD is measured by linear regression of the 14 individual station values up to 589 m a.s.l.. This is justifiable if the water vapour profile is near uniform over this elevation interval, as it is for example up to the LCL in Fig.7. In the following we assume linearity of the lapse rate up to 1083 m a.s.l. The measured departures from linearity are assumed to be caused by horizontal differences in water vapour delay due to airflow. We wish to capture these lateral variations in ZWD and also vertical modulation of ZWD due to topographic intersection with the water vapour field. A method to achieve this is described in Supplement 1.

4. Surface Topography and Wind

The characteristics of the surface of Montserrat and the COSMO-SkyMed InSAR system (Table.1) place limitations on the satellite observations of water vapour delay.

4.1 Viewing Interval and Geometry

The minimum interval between InSAR imaging using the same orbital geometry is about 12-24 days (Pritchard et al., 2018). COSMO SkyMed has a constellation of four satellites and so more frequent revisits were achieved on Montserrat: at intervals of 1- and 4-days. We used seven images (of sufficiently high quality) here, on 2, 3, 6, 10, 14, 18 and 19 December 2014. Two other images were supplied but were too decorrelated to form good quality interferograms. The imaging paths of the COSMO-SkyMed radar are far from vertical and both the resultant slant paths through the troposphere must be simulated in the WMM to give the slant wet delay (SWD). The ascending pass images look at the surface more steeply (26.6° from vertical) than the descending pass images (59.2° from vertical) (Figs.2c, 11). Thus, the radar paths through the ABL are longer for descending passes than for ascending passes. This would have no effect if the 3D water vapour fields were identical at the times of the two images forming the interferogram. But generally, temporally separated water vapour fields do vary spatially (e.g. Minder et al. 2013), so that we would expect the longer paths of the descending pass interferograms to create more spatial variance in the resulting delay fields. The mountain axis of Montserrat is oriented about 350°, roughly perpendicular to the usual easterly trade wind direction. This is also perpendicular to the azimuth of the radar look direction in the ascending pass but about 20° off the perpendicular for the descending pass (Fig.2c). Water vapour-derived variability should increase in descending pass interferograms as the radar path becomes more oblique to the mountain axis of the island and a longer path over the land surface with its high variability of water vapour. So, from both these geometrical effects we would expect the descending pass interferograms to show a greater amplitude of phase variance than for the ascending pass ones, other factors being equal.

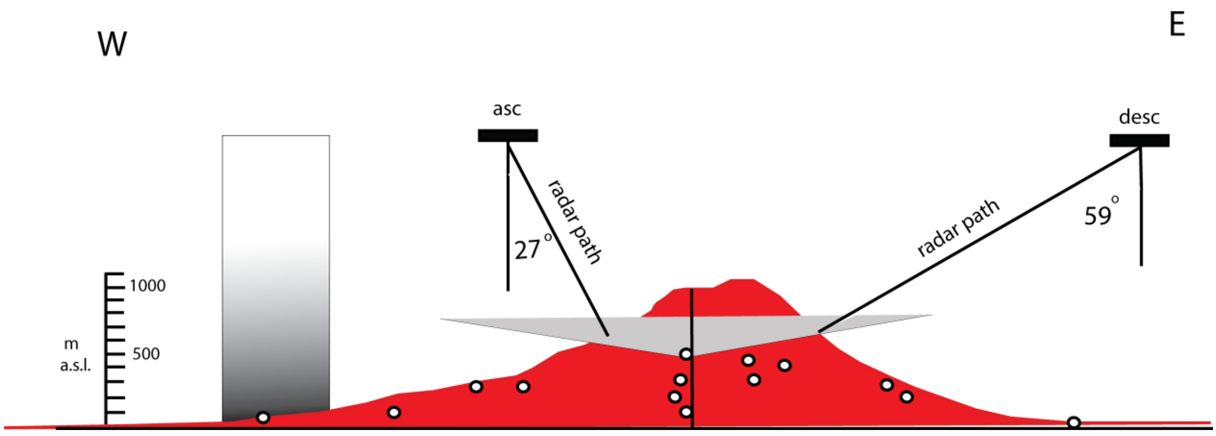

Fig.10 True scale cross section (W-E) through Montserrat at SHV (the location shown in Fig.2c). The ascending (27 degrees from vertical) and descending (59 degrees from vertical) radar slant paths are shown schematically. On the western side of the section is a gradational column schematically intersected by the surface of the SHV volcano. This is shown to emphasize the nature of the problem if the water vapour field is simply layered and the difference between the two can be captured by comparing two static layered fields. The MVO GPS receivers are

shown as black circles plotted in the location of their projection on the section (see Fig.2c for their location in the x,y-plane). Note that there are no receivers above ~ 600 m a.s.l.. The grey triangle represents the apex of the sampling cone forming an angle of 10 degrees above the horizontal for one of the GPS receivers.

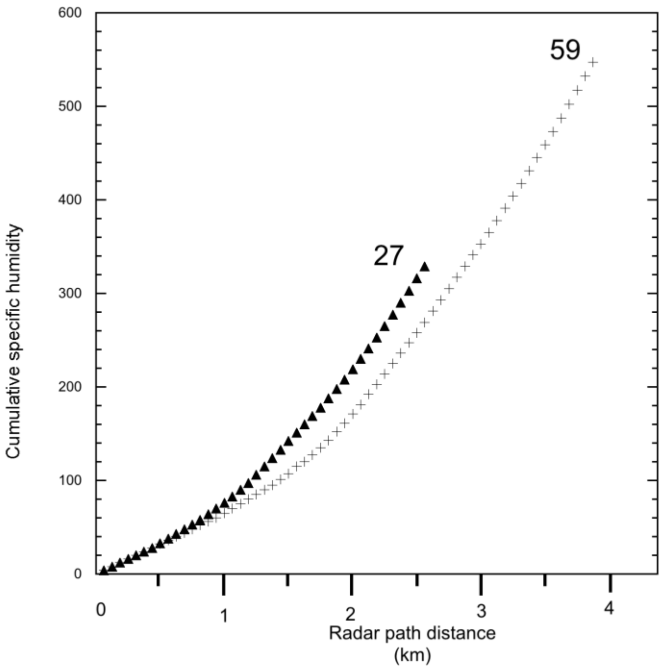

Fig.11 Plot of the cumulative amount of specific humidity water vapour against radar path distance. The origin of the plot lies at a location about 3.5 km above the ground surface. The two curves (labelled 27 and 59) correspond to ascending and descending path satellites respectively, as shown in Fig.10. The two curves are similar until about 800 m when they start to diverge, the ascending path radar encountering water vapour faster until about 2.5 km when it reflects from the ground surface. The descending path radar continues for just over another kilometre until it too hits the surface. The "59" radar records about 1.66 more water vapour than the "27" radar.

4.2 Wind Speed

The speed of the wind has been shown to affect the dynamics of orographic convection in several studies of the atmosphere around the mountains of the Lesser Antilles (Smith et al. 2012; Minder et al., 2013; Cécé et al., 2014). The orientation of convection is highly asymmetric (Nugent et al., 2014). At low wind speeds (<5 m/s) solar surface heating drives convection with surface convergence forming clouds that are slowly moved downstream by the mean wind (Fig.8a). At high wind speeds (>7 m/s) air is forced upward on the windward side forming clouds and high humidity there, whilst to leeward there is plunging flow, reduced cloud formation due to evaporation and reduced water vapour (Fig.8b). We measured the wind velocities during the satellite overpasses (Table 2) from the ground surface near sea level, from an airport anemometer close to the ground surface at about 160 m a.s.l. and from radiosonde observations above Guadeloupe, about 100 km SSE of Montserrat. Following Nugent et al. (2014) we use the average wind in the lower ABL (< 600 m a.s.l.) to determine the tripartite classification of low, medium and high wind speeds. Wind speeds were “low” on 3 and 18 December, “high” on 14 and 19 December and “medium” for the other three days (Table 5) . The wind direction was from east to west for six of the observation days, but with considerable scatter. The wind direction changed from west to east on 6 December during the passage of a low-pressure system to the southeast of Montserrat.

Wadge et al., (2006) collected wind speeds and strength at the time of acquisition of ERS C-band radar images during 1998 – 2000 (Table 4). These show that the eastern quadrant dominated the wind directions and strengths on Montserrat.

Table 4. Wind speed by quadrant at the time of acquisition of ERS C-band images (between March 1998 – November 2000) over the SHV on Montserrat (data from Wadge et al., 2006).

Wind speed (m/s)	North	East	South	West
Low (< 5)	3	1	1	1
Medium (5-7)	1	6	0	0
High (>7)	2	13	2	0

Table 5. Wind observations at the times of imaging in Dec. 2014.

Date	Wind strength	Wind Direction	View/Time[2]
02/Dec/2014	M	East	A
03/Dec/2014	L	East	A
06/Dec/2014	M	West	D
10/Dec/2014	M	Southeast	D
14/Dec/2014	H	Southeast	D
18/Dec/2014	L	East	A
19/Dec/2014	H	East	A

1. H=high (> 7 ms^{-1}), M=moderate (7-5 ms^{-1}), L =low (< 5 ms^{-1})
2. A=ascending pass/sunrise, D=descending pass/sunset

The above evidence shows that strong, easterly winds are most likely to develop strongly asymmetrical convection patterns. We use data from the example of a strong, easterly wind on Dominica modelled by WRF (Minder et al., 2013) shown in Fig.8 which we take to be representative of behaviour at Montserrat. Using the geometry of the east-looking (23^{o}) ascending radar data and the west-looking (59^{o}) descending pass data we find that the water vapour fields detected by the descending pass radar are 1.66 greater than the ascending pass case (Fig.11). It may be possible to extract some simplified states from this asymmetrical behaviour that can be quickly used to predict a 3D water vapour field using ICTZ, trade wind and precipitation, without using a full numerical weather prediction approach.

4.3 Diurnal Cycle

The potential effect of the diurnal cycle on radar refractivity is two-fold. Firstly, the state of the ABL over the island encountered by the radar will depend on the timing of the satellite overpass relative to the cycle (Table 1). In the case of the COSMO-SkyMed data we use, the ascending overpasses of the satellite were at 05:58 local time, just before sunrise at 06:20, at what should be a time of low refractivity noise (Wadge et al., 2016). The descending overpasses were at about 17:34 local time, close to sunset at 17:35, again a time of expected low refractivity noise. On the other hand WRF simulations of sunrise temperatures (e.g. Gonzalez et al., 2013) can show abrupt inflections and noisier behaviour. Secondly, a satellite with an overpass later in the morning, say, could be sampling a much more turbulent ABL than earlier in the cycle after thermal convection had developed. However, if the trade wind speed was high, orographically-forced convection may occur whatever the time of the cycle. The studies of katabatic flow at Guadeloupe (Basse Terre) show that the period from December to March is the most prone to such flows (d'Alexis et al., 2011).

5 Results

5.1 Water vapour fields on individual days

Fig.12 shows radiosonde-derived humidity mixing ratio profiles over land (Guadeloupe) measured at 08:00 local time on the days of radar imaging (within two hours of the ascending pass images on 2, 3, 18 and 19 December and within about nine hours of the descending pass images of 6, 10, 14 December). Overall the humidity mixing ratio profiles have mean values in the range 15-16 g/kg between 0 and 0.6 km altitude. The humidity decreases rapidly and smoothly up to altitudes of about 2 km, above which it falls more slowly up to altitudes of 4–9 km before dropping to values of < 1 g/kg. The individual humidity profiles tend to have characteristics that match the prevailing wind speed. The profiles of 6 and 10 December are very similar with notably more humidity at higher altitudes (4 – 9 km) than on the other days. Both days have a moderate-wind range. The two low-wind days (3 and 18 December) show very similar profiles with high amplitude inversion structures between 2 and 5.5 km. The two high-wind days (14 and 19 December) also have very similar profiles, falling to very low humidity values above 4 km. In figure 13 we compare the WMM ZWD fields with the equivalent ZWD fields derived from GPS at the times of the seven satellite overpasses (Table 1). We can see that the effect of topography in both sets of data is to reduce ZWD value with elevation at both SHV and Centre Hills (Fig.2c), as we expect. The ranges of ZWD values, due to topography, calculated by both methods for the seven days give similar average values: 83 ± 7 mm for GPS and 79 ± 14 mm for WMM. This suggests that both techniques record similar gradients of water vapour content.

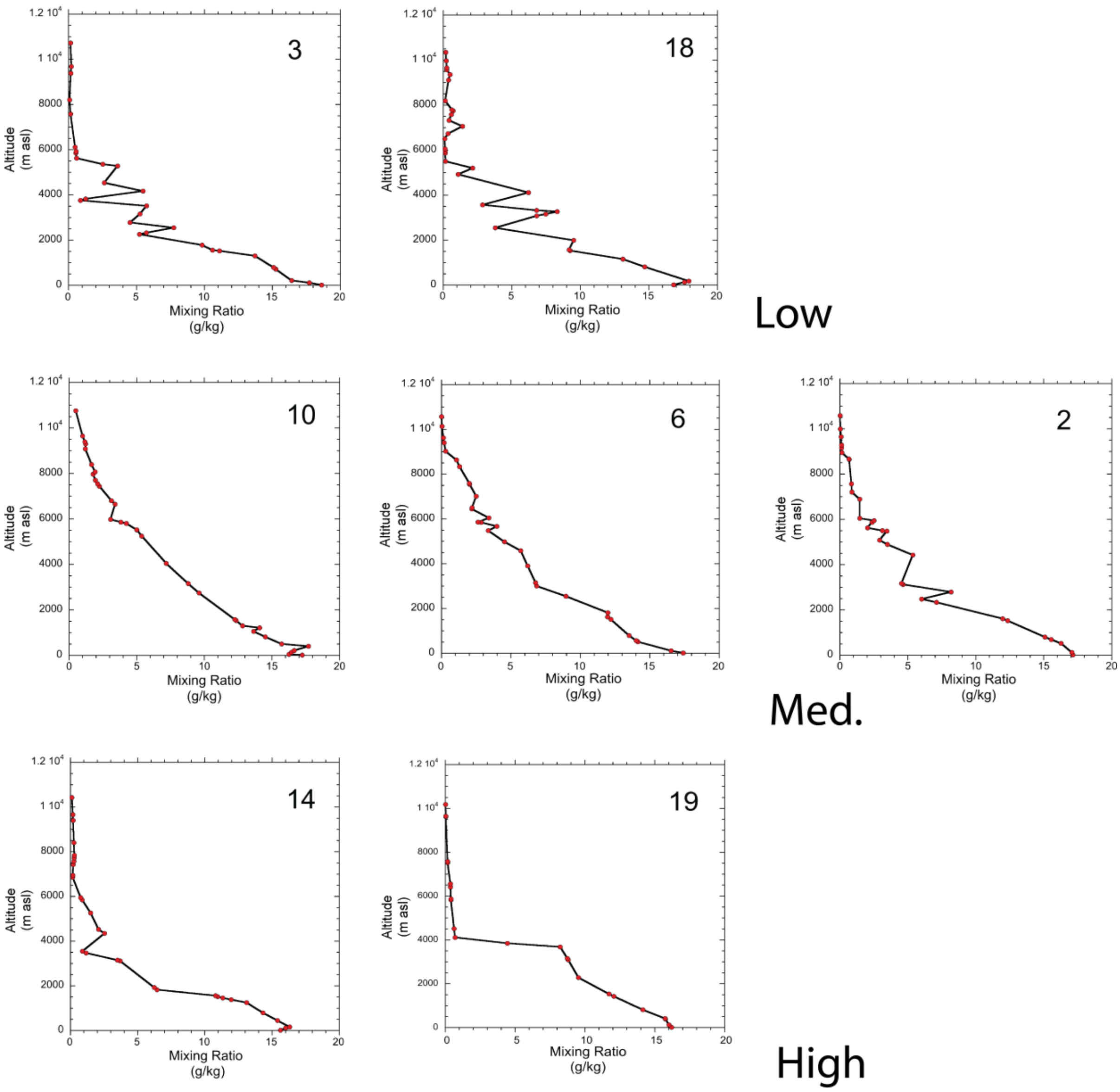

Fig.12 Humidity mixing ratio profiles from radiosondes launched at Le Raiset, Guadeloupe at 08:00 local time on the days of the radar imaging in December labelled in the upper right corner of each panel. Profiles are arranged in high-, medium- and low- wind speed rows.

The absolute values of ZWD from the WMM simulations are generally higher than those from the GPS method: the difference is least on 18 December (15 mm) and most on 14 December (84 mm). When these differences for each of the seven days are plotted against wind speed (Fig. 13 lower left graph), the difference in ZWD values are shown to diverge with increasing wind speed at a rate of about 11 mm/m/s. This bias associated with wind speed is unexpected. The WMM may be lifting too much water vapour from lower levels during high winds. Alternatively, the bias could represent a faulty assumption of the linearity of the water vapour lapse rate in the GPS-based method, for example, in the un-sampled elevation range between about 600 and 1100 m a.s.l. there is a much higher water vapour content at times of high wind speed than expected from a linear extrapolation from lower elevations.

The wind on 6 December was from the west (Table 5), as opposed to the usual easterly trade wind direction. In the WMM simulation (Fig. 13) the low levels of ZWD associated with the SHV topography are displaced to the southeastern corner of the island compared to days when the wind was easterly, for example, on 10 December. This is particularly so for the 19 December case, which had high speed, easterly winds and high ZWD values on the southeast, windward coast, equivalent to the high wind-speed case from Dominica illustrated in Fig.8b. Thus, out of the seven cases, the one with clear evidence of reversed trade wind flow (6 December) generates the expected reversal of ZWD asymmetry in the WMM model.

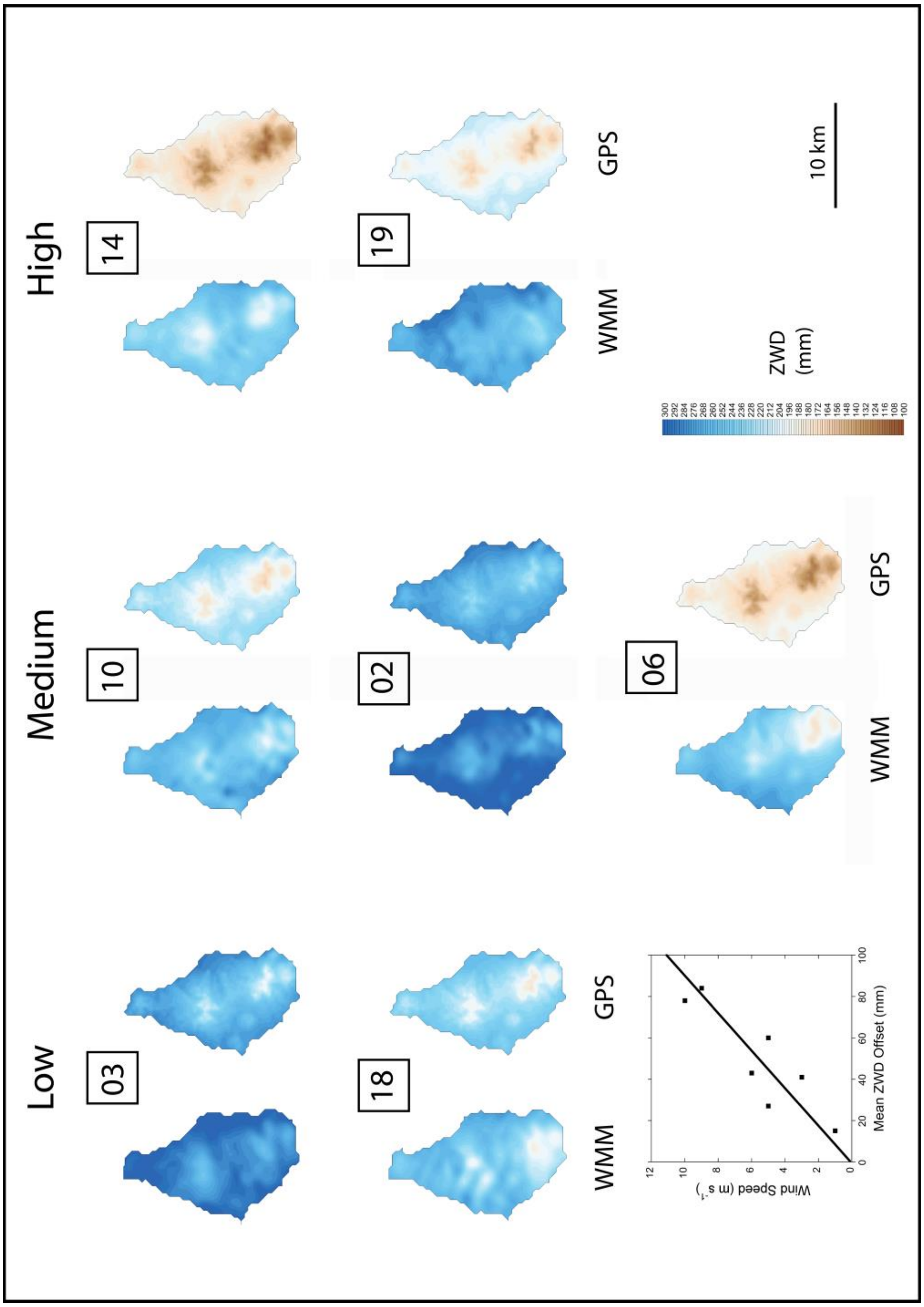

Fig. 13 Pairs of maps of ZWD over Montserrat during December 2014. The date is given by the number between each pair. The left image of each pair is the WMM simulation and the right image is from the GPS method, as described in the text. The pairs are arranged in three columns according to the "low, medium and high" wind speeds on those days (Table 5). The ZWD data are plotted to a horizontal posting of 300 m, the finest model resolution of the WMM. The colour scale of ZWD values shown on

the bottom row is common to both sets. The graph at the bottom left is of ABL wind speed versus the mean offsets in ZWD values between the two methods for the seven days.

5.2 WMM differential water vapour fields at zenith

The radar image pairs: 2-3, 6-10, 10-14, 18-19 December were chosen for interferogram creation. The WMM-derived maps of ZWD differences (earlier – later) correspond to the four intervals (Fig. 14). Firstly, we compare these ZWD differences with those between the integrated humidity mixing ratios determined by radiosonde profiles between 0 and 2 km a.s.l. (Fig. 12), taken to be representative of the humidity in the ABL. These differential values are: 02-03 = +1.4, 06-10 = -3.5, 10-14 = +5.4 and 18-19 = 0.0 g/kg. The positively-valued pairs (02-03 and 10-14) show similarly valued ZWD (Fig.14) whilst the negatively-valued pair (06-10) corresponds to mainly negative ZWD values and the 18-19 pair is dominated by negative ZWD values unlike the radiosonde pair (0 g/kg). Secondly, we assess the spatial patterns of Fig.14. The 2-3 field is of low amplitude with negative values in the east and positive values in the west. A similar pattern is seen in the 6-10 field, except for much larger negative values on the southeast coast. This is the same WMM-derived feature discussed above and as seen in Fig.13 which is probably the result of westerly winds on 6 December and easterly winds on 10 December, shifting the low ZWD values above the volcano from the east on the 6 December to the west on the 10 December. The 10-14 field is largely positive, with much more humid values on 10 December. In contrast, the 18-19 field is dominantly negative with generally more humid values on the 19th relative to the 18th. Both the 10-14 and the 18-19 difference fields have most of their variability at the 1 km scale rather than the island-scale patterns of 2-3 and 6-10, perhaps due to model convection noise driven by high wind speed on 14 and 19 September.

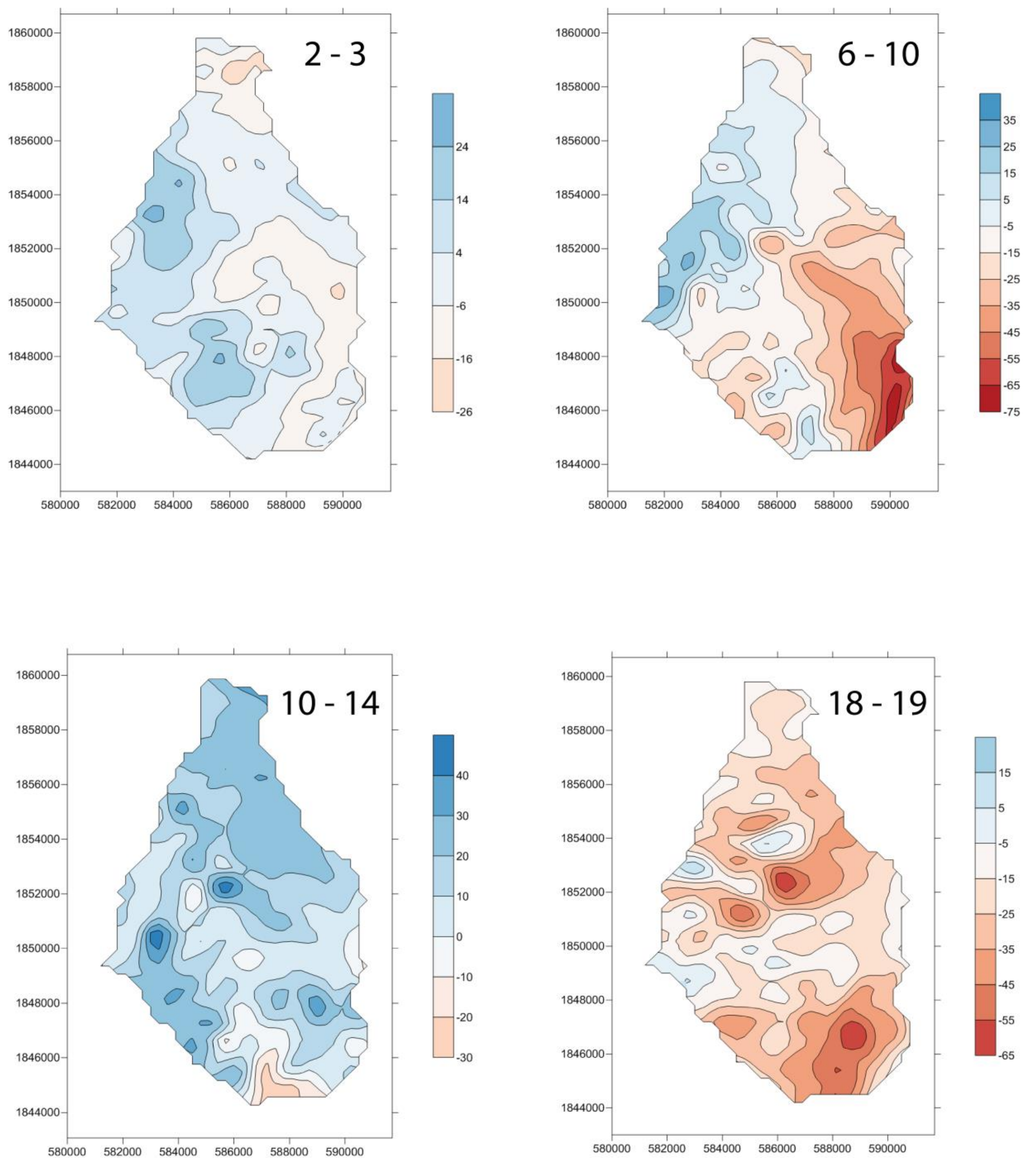

Fig. 14 *WMM-derived ZWD difference fields for four pairs of dates corresponding to the interferograms. Differences in mm (earlier-later). Time intervals in December (days) are given in the top right of each panel. Local grid values in kilometres. Values in lower corner boxes are the rms delay values also shown in Table 6.*

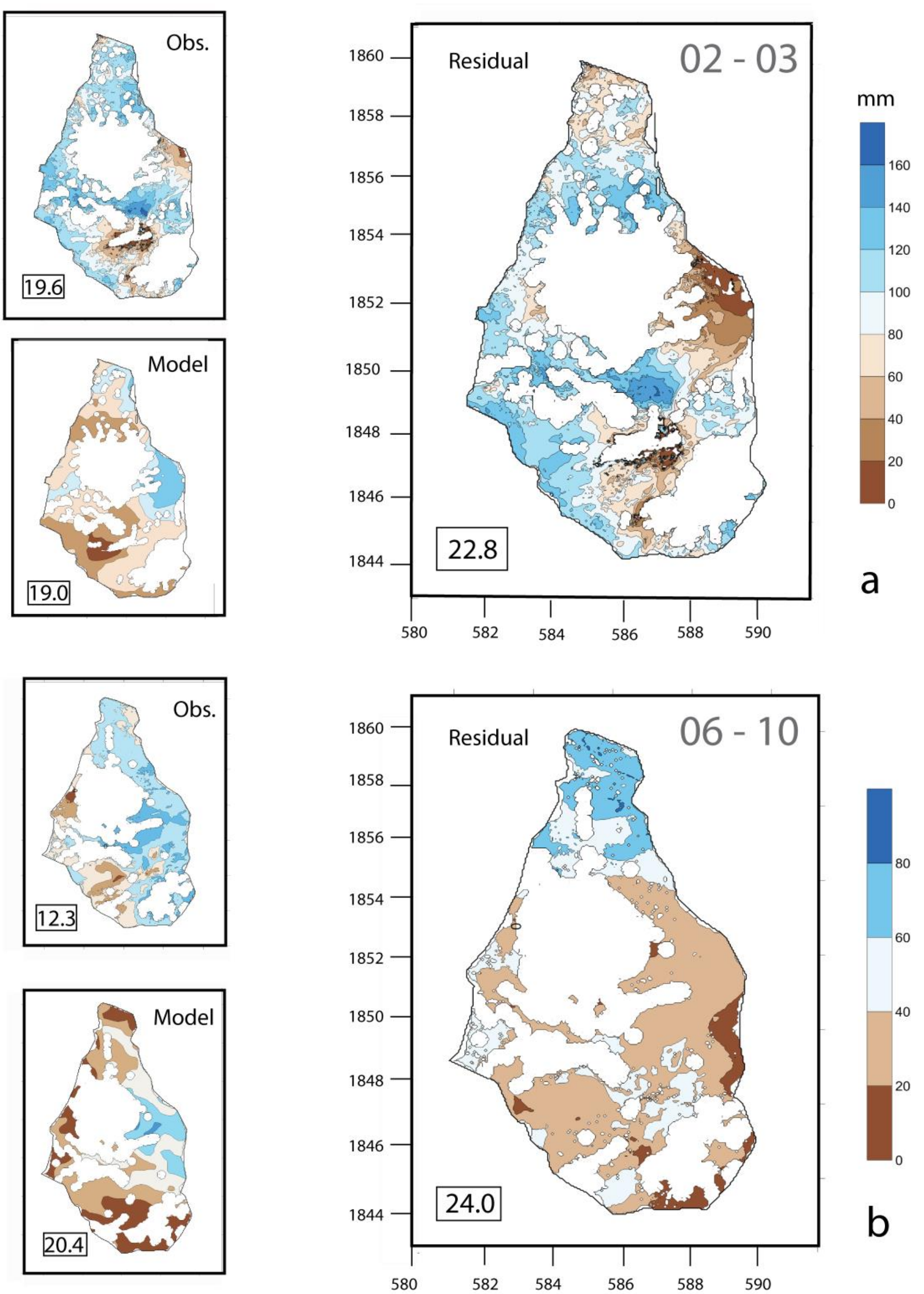

Fig.15 Slant wet delay fields for observed (Obs.) interferogram data, modelled (Model) WMM data and the Residual (Observed – Modelled) fields for (a) the 2-3 December and (b) the 6-10 December intervals. Differences in mm (earlier-later). Local grid values in metres. Values in lower corner boxes are the rms delay values also shown in Table 6.

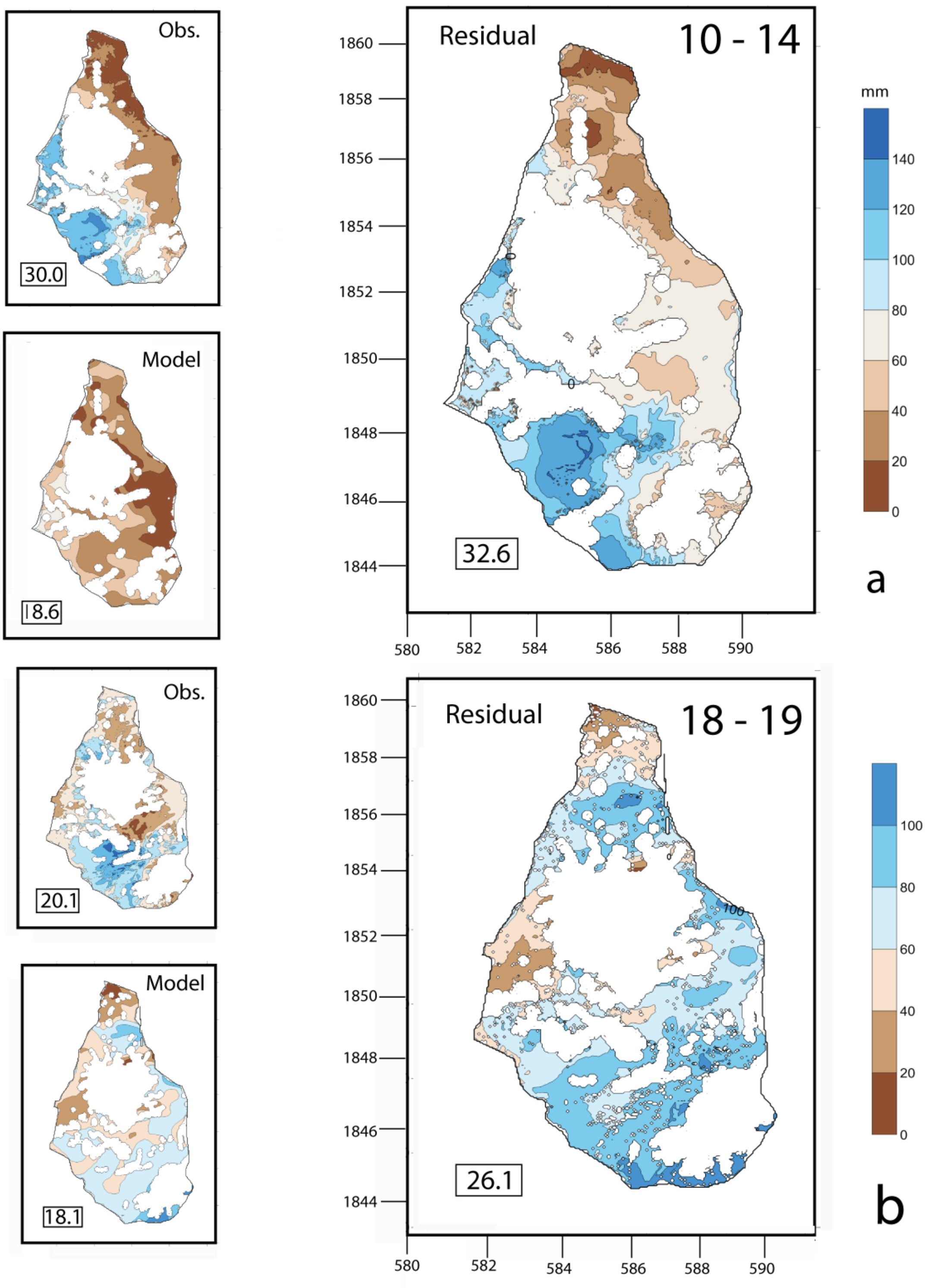

Fig.16 Slant wet delay fields for observed (Obs.) interferogram data, modelled (Model) WMM data and the Residual (Observed – Modelled) fields for (a) the 10-14 December and (b) the 18-19 December

intervals. Differences in mm (earlier-later). Local grid values in kilometres. Values in lower corner boxes are the rms delay values also shown in Table 6.

5.4 Differential InSAR - WMM slant fields

We now consider the observed delay fields of the COSMO-SkyMed pairs. Specifically, along the slant of the radar paths, 26.6° and 59.2° from zenith. The residual fields created by subtracting the WMM – SWD field from the equivalent field observed by COSMO-SkyMed, including the incoherence masks, are shown in Fig.s 15, 16. The observed and modelled fields are quite similar for 06-10, 10-14 and 18-19 periods, but not for 02-03.

2 – 3 December

The only obvious feature in common between the observed and modelled delay fields is that the lowest differences are seen around the upper slopes of the volcano. Generally, elsewhere the modelled differences are smaller than the observed differences. The overall range of differences is greatest in this pair of dates.

6 - 10 December

The observed and modelled SWD fields show similar patterns. In the observed field there is a strong gradient across the island with the eastern side of the island having the greatest differences and the south-western side the least change across the two dates. This is also seen in the model results but for a more restricted area on the middle, leeward slopes. The northernmost part of the island shows a contrasting pattern with the highest residuals.

10 – 14 December

The observed SWD field shows a strong gradient of water vapour, high in the southwest, low in the northeast. The modelled version is similar but of a smaller magnitude. The pattern of differences for these 5 days is a reversal of that shown by the 6-10 December interferogram, with a lowest difference on the eastern slopes. This suggests a source that is the common date (10 December) shared by the two intervals. The model field has the smallest range. The humidity mixing ratio is considerably greater on 10 December that on 6 or 14 December (Fig.12), with an inversion horizon 2 km higher than that of 14 December (4 km).

18 – 19 December

On these two days the phase differences were similar in both observed (InSAR) and model, high in the south of the island and low in the north, though the WMM range is generally lower than the InSAR result.

The range of values in the observed and modelled delay fields is similar, approximately 80-120 mm. The two descending pass interferograms (06-10 and 10-14) show strong ENE-WSW gradients across the island (Figs.15, 16) with opposite polarities. The two pairs share the same 10 December image, which is the most likely explanation for this pattern. The two ascending pass delay fields (02-03 and 18-19) have shorter intervals (1-day) but less distinct gradients matching the trade wind orientation.

The WMM model delay fields show some structural similarities to those observed by radar. For example, the 06 -10 WMM field shows higher delay values (more water vapour) in the central windward side of the island, as does the observed field. The WMM field for 18-19 December shows a lower delay value (less water vapour) in the northern half of the island compared to the radar-derived field. The radar fields across the highest parts of SHV tend to show the strongest gradients, suggestive of the abrupt change in flow regime across the island's topographic divide as shown in Fig.9 b. This is also seen in some of the WMM fields as in 02-03 and 06-10, but the gradient is less steep.

The effectiveness of reducing the atmospheric component of phase delay in the interferograms is assessed by calculating the root mean squared (RMS) error and the percentage of pixel delay (PPD) between the interferograms and the WRF simulations across the island (Table 6). PPD is defined here as the pixel-wise offset in the difference field from zero expressed as a percentage, where 100% would mean a difference field at zero (perfect match) and 0% would mean all pixels in the difference image would exceed the maximum bounds of the residual image. We expect a small delay RMS and a high PPD if WRF performs well. The RMS of the radar interferograms has a mean value of 20.5 mm, less than that of the residual, 26.4 mm Using the PPD metric the 06-10 value has the most accurate residual of 80.95%, values for 6-10, 10-14 and 18-19 intervals of 80.9%, 65.42% and 76.82% respectively.

Table 6. RMS delay differences for image interferograms with ambient wind speed.

Dates for each pair	COSMO-SkyMed (mm)	WMM (mm)	Residual (mm)	PPD % (mm)	Average daily wind speed difference (m/s)	Wind comments
2 -3/Dec/2014	19.58	19.01	22.78	64.51	4.8	More E-W flow than S-N
6–10/Dec /2014	12.29	20.41	24.03	80.95	9.5	Strong E-W flow, little S-N flow
10/14/Dec//204	30.05	18.64	32.61	65.42	6.7	Strong S-N flow
18/19/Dec/2014	20.14	18.10	26.06	76.82	2.7	Similar S-N flow to E-W

Table 7 shows the relative proportions of slant wet delay (SWD), liquid wet delay (LWD) and hydrostatic delay (HSD) calculated from the WMM difference fields corresponding to the dates of the four interferograms. LWD is calculated using the delay coefficient for cumulus cloud from Hanssen, (2001), that is the most appropriate (0.7). As expected, SWD is about an order of magnitude larger than LWD and HSD values. December is just

Table 7. Percentage differences of total delay within the WMM apportioned to Slant Wet Delay (SWD), Liquid Water Delay (LWD) and Hydrostatic Delay (HSD).

Dates	SWD %	LWD %	HSD %
2 – 3/Dec/2014	81.9	11.3	6.8
6 – 10/Dec/2014	86.5	9.5	4.0
10 – 14/Dec/2014	88.0	7.1	4.9
18 – 19/Dec/2014	84.7	9.8	5.4

after the end of the wet season in Montserrat (Fig.4). Images of precipitation from the TRMM satellite show that the only regional rainfall over the period occurred on 6 December during the passage of a mesoscale feature that skirted Montserrat to the south and also produced westerly winds. The proportion of LWD (11 - 7 %), generally derived from the WMM, is not negligible.

6. Discussion

6.1 Understand where and when tropical water vapour originates.

The tropics contain the highest levels of atmospheric water vapour as it evaporates above warm ocean. Our test case SHV volcano, Montserrat lies in the western tropical Atlantic and is subject to the migration of the ITCZ, northwards during the wet season and southwards in the dry season. The main effect of the ITCZ is to cycle rainfall and precipitable water vapour, in the case of Montserrat causing rainfall rates of about 1 mm/day in the dry season to about 5 mm/day in the wet season. Because of its differential nature, InSAR will tend to give the largest atmospheric signals, with one image from the peak and one from the trough of the ITCZ cycle (e.g. Fig.3). A detailed study of the same effect from Fogo volcano in the eastern tropical Atlantic (Heleno et al., 2010) indicates about 50-30 mm of phase change could be possible at Montserrat, similar to the findings of Wadge et al. (2006). Also the tropical seas of southeast Asia contain a large number of volcanoes, many on islands, that are affected by the ITCZ. The periodicity and amplitude of the ITCZ humidity signal (Martinez et al., 2019; Pausata and Camargo, 2019) are well characterized and hence provide a way to estimate the local scale of water vapour forcing as it affects InSAR on volcanoes.

6.2 Measure and simulate water vapour over a small mountainous tropical volcano

There is no easy way to separate the phase delay differences of the two images contributing to the interferogram once its components are combined. Typical ranges of water vapour content variation across Montserrat are about 100 mm. The humidity mixing ratios increase from ~5 - 1 g/kg at the top of the ABL (~2 - 4 km altitude) to about 18 g/kg at sea level. (Fig.12)

In our experiment we used X-band radar in both ascending and descending paths. The ascending path of the satellites follow an azimuth of 349° at an angle of about 27° to the zenith and the descending path an azimuth of 011° and an angle of about 59° to the zenith. As a result, the length of the descending path through the troposphere is about 1.7 greater than that experienced by the ascending path. The water vapour encountered should be equivalent to this ratio if the path has equivalent specific humidity. The horizontal orientation of the mountain chain forming Montserrat is about 350°, roughly parallel to the ascending radar path, whilst the descending radar path, is oriented about 20° anticlockwise to the topographic axis. The WMM has 5 nested levels, the first 0.3 km grid being the one that just covers Montserrat. Whilst this 300 m scale is adequate for many applications, it is of less value at representing convection simulating clouds, such as the growth of clouds above a heated ground surface (Kirshbaum and Smith, 2009).

6.3 Show how model and observational variations of humid flow depend on the scale and setting of this flow.

The direction and speed of the winds, the orientation of the topography, and the diurnal cycle of water vapour are major factors in controlling humid flow. Trade winds blowing from the east dominate in Montserrat. These winds tend to produce asymmetrical humidity fields, with higher values over the windward (eastern) slopes and lower values on the leeward (west) side, particularly when the wind speed is high (>7 m/s). Lee waves tend to form on the leeward side with cloud enhancement and precipitation. At lower wind speeds diurnal solar heating tends to form above hot land surfaces with long trails of clouds converging downwind about 30-40% of the time (Kirshbaum and Fairman, (2015). Out of the 7 days of radar measurements, one (6 December) experienced wind from the west (due to a regional system to the southeast). This had a clear impact on the humidity field, creating low specific humidity over the south-eastern flank of the island (Figs. 13,14). The asymmetry of the humidity field during normal trade wind days produces specific humidity values that are greater on the windward relative to the leeward side.

Accurate WMM slant delay fields should be identical to those of the contemporaneous interferograms. However, they differ quite significantly as seen in Figs. 15, 16 and Table 6. The standard deviations of the residual images are marginally greater than those of the WMM and InSAR images (Table 6). Spatial offsets of only a few hundred metres in these models are sufficient to generate large local gradients in the humidity fields, e.g. Fig. 16. This misfit has been observed in other interferogram-based studies (e.g. Bekaert et al., 2015). It was thought that the relatively high resolution of the WMM would help mitigate this. But perhaps the 300 m horizontal resolution of the model was still too coarse to capture the flow modifying terrain sufficiently well. The lack of detail in the WMM (300 m resolution) is an explanation of why the range of model specific humidity values tend to be less than the InSAR measurements (~2m resolution). In order to capture finer details in the dynamic water vapour profile, alternative approaches, or a hybrid of them, may be adopted such as the use of large-eddy simulation (Kirshbaum and Smith, 2009), statistical models or empirical image processing techniques – although these techniques present their own problems.

7. Conclusion

Unknown amounts of water vapour in the troposphere introduces error in the measurement of geodetic signals, particularly at volcanic islands such as Montserrat. Using InSAR (and GNSS) measurements and WRF modelling, at the time of the overpasses of radar-bearing satellites, we examined the temporal and spatial factors leading to the variability of water vapour. The dominant process that controls the annual water cycle at Montserrat is the ITCZ. This brings an irregular annual dynamic behaviour of water vapour, rainfall and winds. Low values of water vapour occur during the boreal winter and spring and high values in the boreal summer and autumn. The range of specific humidity measured globally by the ITCZ is about 6 g/kg, consistent with that measured locally at Montserrat (and Fogo). Improved knowledge of the ITCZ's climatology and local behaviour would help to forecast water vapour error budgets.

Another important factor after water vapour distribution is the trade winds. In the vicinity of the eastern Caribbean the trade winds blow from the east northeast. This is often modified as the ITCZ passes the equator with east southeast flow at higher speeds in summer. Occasionally, the flow is markedly changed or entirely reversed by regional features. This occurred during one day of our experiment (6 December) in which the island-wide wind pattern was reversed. It produced a weak westerly flow and concentration of water vapour in the west, the opposite of the “normal” trade wind pattern.

Most days the rising sun coincides with strong surface heating and the ensuing development of both maritime and terrestrial-generated convection. This in turn is susceptible to modification by the local strength of the trade winds and even-more localised convection effects associated with topography. For example, at SHV, several 100 m scale circular refractive phase anomalies are evident as features that wax and wane with the diurnal cycle (Wadge, et al., 2016).

Acknowledgements

This work was supported by NERC grant NE/H019928/1 to GW with support from COMET. TW is grateful for the NERC studentship NE/J500082/1. The COSMO-SKYMED radar data were supplied by the Italian Space Agency under a CEOS scheme and we thank M. Pritchard for his help in this regard. We acknowledge the radiosonde data came from the archive of the Department of Atmospheric Sciences, University of Wyoming, the numerical model initial condition data came from the ECMWF, Thomas Christopher at the Montserrat Volcano Observatory provided a climatology dataset and Prof. Daniel Kirshbaum gave access to Fig. 8a. Thanks, also, to Dr. Chris Holloway. The manuscript was greatly improved following comments by four referees and the RSE editing team.

References

Alshawaf, F., Hinz, S, Mayer, M., Meyer, F.J. (2015) Construction accurate maps of atmospheric water vapour by combining interferometric synthetic aperture radar and GNSS observations. *J. Geophys Res*., 120/1391-1403, doi:10.1002/2014JD022419.

Barclay, J., Johnstone, J.E., Matthews, A.J. (2006) Meteorological monitoring of an active volcano: implications for eruption prediction. *J. Volcanol., Geotherm. Res.*, 150, 339-358.

Bekaert, D.P.S. Hooper, A., Wright, T.J (2015) A spatially variable power law tropospheric correction technique for InSAR data. *J. Geophys. Res.*, 120, 1345-1356, doi: 10.1002/2014JB011558.

Bekaert, D.P.S. Walters, R.J., Wright, T.J., Parker, D.J. (2015) Statistical comparison of InSAR tropospheric correction techniques, *Rem. Sensing Env*., 170, 40-47.

Bengtsson, L. (2010) The global atmospheric water cycle. *Env. Sci., Lett*., 5, 025202.

Bennitt, G. and Jupp, A. (2012) Operational assimilation of GPS zenith total delay observations into the Met Office Numerical Weather Prediction Models. *Monthly Weather Rev*., 140, 2706-2719.

Bevis, M., Businger, S., Herring, T.A., Anthes, R.A., Wadre, R.W. (1994), GPS meteorology: mapping zenith wet delays onto precipitable water. *J. Appl. Meteor.* 33(3), 379-386.

Boehm, J., Niell, A., Tregoning, P., Schuh, H., (2006) Global mapping function (GMF): a new empirical mapping function based on numerical weather model data. *Geophys. Res. Lett*., doi: 10.1029/2005GL025546.

Boehm, J. Heinkelmann, R. Schuh, H. (2007) Short Note: A global model of pressure and temperature for geodetic applications. *J. Geod*., 81, 679-683.

Cécé, R., Bernard, D, D’Alexis, C., Dorville, J-F. (2014) Numerical simulations of island-induced circulations and windward katabatic flow over the Guadeloupe Archipelago. *Monthly Weather Rev*., 142, 850-867.

Costantini, M. (1998) A novel phase unwrapping method based on network programming. *IEEE, Trans. Geosci., Rem. Sens*., 36/3, 813-821.

D'Alexis, C., Abouna, A., Berthelot, H., Bernard, D. (2011) Characteristics of nocturnal breezes in the Windward Islands in the southeastern Caribbean: structure and night-time regimes. *J. Caribbean Acad. Sci.,* 5(2).

Davison, J.L., Rauber, R.M., Di Girolamo, L., LeMone, M.A. (2013) A revised conceptual model of the tropical marine boundary layer, Part I: statistical characterization of the variability inherent in the wintertime trade wind regime over the western tropical Atlantic. *J. Atmos. Sci*., 70, 3005-324.

Ebmeier, S.K. and co-authors (2018) Synthesis of global satellite observations of magmatic and volcanic deformation: implications for volcano monitoring and the lateral extent of magmatic domains. *J. App. Volcanol*., 7:2, doi: 10.1186/513617-018-0071-3.

Elliott, J.R., Biggs, J., Parsons, B. Wright, T.J. (2008) InSAR slip rate determination on the Altyn Tagh Fault, northern Tibet, in the presence of topographically correlated atmospheric delays. *Geophys, Res. Lett*., 35, L12309, doi: 10.1029/2008GL033659

Fattahi, H., Amelung, F. (2014) Insar uncertainty due to orbital errors. *Geophys. J. Int*., 199/1, 549-560.

Fattahi, H., Simons, M., Agram, P., (2017) InSAR time-series estimation of the ionospheric phase delay: an extension of the split range-spectrum technique., *IEEE, Trans., Geosci, Rem, Sens*., 55/10, doi: 10.1109/TGRS.2017.2718566.

Hanssen, R.F. (2001) *Radar Interfeometry*. *Data interpretation and error analysis*. Kluwer Academic Publishers,, Dordrecht, 308 pp.

Feng, J., Zhen, W., Wu, Z. (2017) Ionospheric effects on repeat-pass SAR interferometry. *Adv. Space Res.*, 60, 1504-1515, doi: 10.1016/j.asr.2017.06.019.

Herring, T.A., King, R.W., Floyd, M.A. and McClusky, S.C. (2010a) GAMIT Reference Manual, GPS Analysis at MIT. *Department of Earth, Atmospheric and Planetary Sciences, Massachussts Institute of Technology, Cambridge, USA.*

Herring, T. A., Floyd, M.A., King, R. W., and McClusky, S. C. (2010b) GLOBK reference manual, Global Kalman filter VLBI and GPS analysis program. *Department of Earth, Atmospheric, and Planetary Sciences, Massachusetts Institute of Technology, Cambridge*. *USA.*

Hofmann-Wellenhof, B., Lichtenegger, H., Collins, J. (1995) Global Positioning System, Theory and Practice, *3rd edition, Springer-Verlag, Wien*.

Goldstein, R.M. and Werner, C.L. (1998) Radar interferogram filtering for geophysical applications. *Geophys.*, *Res.*, *Lett*., 25/21, 4035-4038,10.1029/95GL900033.

Gonzalez, A., Exposito, F.I., Perez, J.C., Diaz, J.P., Taima, D. (2013) Verification of precipitable water vapour in high resolution WRF simulations over a mountainous archipelago. *Q. J. R. Meteorol., Soc.*, 139:2119-2133.

Heleno, S.I.N., Frischknecht, C., d'Oreye, N., Lima, J.N.P., Faria, B., Waff, R., Kervyn, F. (2010) Seasonal tropospheric influence on SAR interferograms near the ITCZ- the case of Fogo Volcano and Mount Cameroon. *J. African Earth Sci.*, 58/5 833-856. 10.1016/j-jafreasci, 2009-07-013.

Li, Z., Fielding, E., Cross, P., Muller, J-P., (2005) InSAR atmospheric correction – GPS topography-dependent turbulence model (GTTM). *J. Geophys. Res*., 110, B02404, doi: 10.1029/2005JB003711.

Li, Z., Cao, Y., Wei, J., Duan, M., Wu, L., Hou, J., Zhu, J., (2019) Time series InSAR ground deformation monitoring: atmospheric delay modelling and estimating. *Earth Sci. Rev.,* 192, 258-284.

Jolivet, R., Grandin, R., Lasserre, C., Doin, M-P., Peltzer, G., (2011) Systematic InSAR tropospheric phase delay corrections from global meteorological reanalysis data. *Geophys., Res., Lett.*, 38, L17311 doi: 10.1029/2011GL 048757.

Jolivet, R., Agram, P.S., Lin, N.Y., Simons, M., Doin, M.P., Peltzer, G., Li, Z. (2014) Improving InSAR geodesy using global atmospheric models. *J. Geophys., Res.*, 119(3), 2324-2341.

Kirshbaum, D.J., Durran, D.R. (2004) Factors governing cellular convection in orographic precipitation. *J. Atmos. Sci.*, 61, 682-698.

Kirshbaum, D.J., Smith, R.B. (2009) Orographic precipitation in the tropics: large-eddy simulations and theory. *J. Atmos. Sci.*, 66, 2559-2578.

Kirshbaum, D.J., Fairman Jr., J.G. (2015) Cloud trails past the Lesser Antilles. *Monthly Weather Rev.*, April 2015, 995-1017.

Kirshbaum, D. J., (2017) On upstream blocking over heated mountain ridges. *Q. J. R. Meteorol. Soc.*, 143: 53-68.

Laderach, A., Raible, C.C., (2013) Lower troposphere humidity: climatology, trends and the relation to the ITCZ. *Tellus A*, 65, 20413, doi10.3402/tellus v.6510.20413.

Lager K., Schindelegger M., Bohm J., Krasna H., Nilsson T (2013) GPT2: Empirical slant delay model for radio space geodetic techniques. *Geophys. Res. Lett*. 40,6, 1069-1073.

Lu, Z., Dzurisin, D. (2014) *InSAR imaging of Aleutian Volcanoes*, Springer, New York, pp.390.

McVicar, T.R. and Korner, C. (2013) On the use of elevation, altitude and height in the ecological and climatological literature. Oecologia, 171, 335-357. Doi: 10.1007/S00442 – 012-2416-7.

Massonnet, D. and Feigl, K. (1998) Radar interferometry and its application to changes in the Earth’s surface. *Rev. Geophys.*, 36, 441-500.

Matthews, A.J., Barclay, J., Carn, S., Thompson, G., Alexander, J., Herd, R.A., Williams, C. (2002) Rainfall-induced volcanic activity on Montserrat. *Geophys. Res. Lett*., 29, (130), 1644, doi:10.1029/2002GL014863.

Martinez, C., Goddard, L., Kushnir, Y., Ting, M. (2019) Seasonal climatology and dynamical mechanisms of rainfall in the Caribbean. *Climate Dynamics*, doi: 10.1007/s00382-019-04616-4.

Minder, J.R., Smith, R.B., Nugent A.D. (2013) The dynamics of ascent-forced orographic convection in the tropics: results from Dominica. *J. Atmos. Sci*., 70, 4067-4088.

Munoz, E., Busalacchi, A.J., Nigam, S., Ruiz-Barradas, A. (2008) Winter and summer structure of the Caribbean Low-Level Jet., *J. Climate*, 21/1260-1276.

Nugent, A.D., Smith, R.B., Minder, J.R. (2014) Wind speed control of tropical orographic convection. *J. Atmos. Sci*., 71, 2695-2712.

Odbert, H.M., Ryan, G.A., Mattioli, G.S., Hautmann, S., Gottsmann, J., Fournier, M., Herd, R.A., (2014) Volcanic geodesy at Soufriere Hills Volcano, Montserrat: a review. From: Wadge, G., Robertson, R.E.A., Voight, B. (eds.) The eruption of Soufriere Hills Volcano, Montserrat from 2000 to 2010. Geol. Soc. London, Memoirs, 39, 195-217. doi/101144/M39.11.

Pausato, F.S.R., Camargo, S.J. (2019) Tropical cyclone activity affected by volcanically induced ITCZ shifts. *PNAS*, 116/16 , doi:10.1073/pnas.1900777116.

Poulidis, A.P., Renfrew, I.A., Matthews, A.J. (2016) Thermally induced convective circulation and precipitation over an isolated volcano. *J. Atmos. Sci.*, April 2016. Doi: 10.1175/JAS-D-14-0327.1.

Pritchard, M. E. and co-authors (2018) Towards coordinated regional multi-satellite InSAR volcano observations: results from Latin America pilot project. *J. App. Volcanol*., 7:5 doi/10.1186/513617-018-00746.

Richter, I., Xie, S-P., Morioka, Y., Doi, T., Taguchi, B., Behera, S., (2017). Phase locking of equatorial Atlantic variability through seasonal migration of the ITCZ. *Clim. Dyn*., 48, 3615-3289.

Siebsma, A.P., Bretherton, C.S., Brown, A., Chlond, A., Cuxart, J., Duynkerke, P.G., Jiang, H., Khairoutdinov, M., Lewellen, D., Moeng, C-H, Sanchez, E., Stevens, B., Stevens, D.E. (2003) A large eddy simulation inter-comparison study of the shallow cumulus convection. *J. Atmos. Sci*., 60/10, 1201-1219.

Schneider, T., Bischoff, T., Haug, G.H. (2014) Migrations and dynamics of the Intertropical Convergence Zone. *Nature, Review*.513, 45-53.

Skamarok, W.C., and co-authors (2008) A description of the Advanced Research WRF version 3. *NCAR Tech. Note NCAR/TN-475+STR*, 113 pp.

Smith, R.B., Gleason, A.C., Gluhosky, P.A., Grubisic, V. (1997) The wake of St Vincent. *J. Atmos. Sci*., 54, 606-623.

Smith, R.B., Minder, J.R., Nugent, A.D., Storelvmo, T., Kirshbaum, D.J., Warren, R., Lareau, N., Palany, P., Arlangton, J., French, J. (2012) Orographic precipitation in the tropics. *Bull. Am. Meteor. Soc*., October, 2012,1567-1579.

Spaans, K., Hooper, A., (2016) InSAR processing for volcano monitoring and other near real-time applications. *J. Geophys. Res.: Solid Earth*, 121,2947-2960. 10.1002/2015JB012752.

Stevens, B., (2006) Bulk boundary-layer concepts for simplified models of tropical dynamics. *Theor. Comput. Fluid Dyn*. 20, 279-304.

Stinton A., Bass V., Christopher T., Edgecombe N., Fergus M., Pascal K., Smith P., Stewart R., Syers R., Williams C. (2016) MVO Scientific Report for Volcanic Activity between 1 October 2015 and 30 April 2016, *Montserrat Volcano Observatory Open File Report OFR 16-02*.

Stull, R.B., (1988) *An introduction to boundary layer meteorology*. Springer, Heidelberg, 666 pp.

Taylor, M.A., Alfaro, E.J. (2005) Climate of Central America and the Caribbean. In: *Oliver J.E., Encyclopedia of World Climatology*. Encyclopedia of Earth Sciences series. Springer, Dordrecht.

Wadge, G., Webley, P.W., James, I.N., Bingley, R., Dodson, A., Waugh, S., Veneboer, T., Puglisi, G., Mattia, M., Baker, D., Edwards, S.C., Edwards, S.J., Clarke, P.J. (2002) Atmospheric models, GPS and InSAR measurements of the tropospheric water vapour field over Mount Etna. *Geophys. Res. Lett*., 29/19, 11-1 - 11-4, doi: 10.1029/2002GL015159.

Wadge, G., Mattioli, G.S., Herd, R.A. (2006) Ground deformation at Soufriere Hills Volcano, Montserrat during 1998-2000 measured by radar interferometry and GPS. *J. Volcanol. Geotherm. Res*., 152/1-2, j.jvolgeores,205.11.007.

Wadge, G., Zhu, M., Holley, R.J., James, I.N., Clark, P.A., Wang, C., Woodage, M.J. (2010) Correction of atmospheric delay effects in radar interferometry using a nested mesoscale atmospheric model. *J. App. Geophys*., 72, 141-149.

Wadge, G., Voight, B., Sparks, R.S.J., Cole, P.D., Loughlin, S.C., Roberston, R.E.A., An overview of the eruption of Soufriere Hills Volcano from 2000 to 2010. From: Wadge, G., Robertson, R.E.A., Voight, B. (eds.) *The eruption of Soufriere Hills Volcano, Montserrat from 2000 to 2010*. Geol. Soc. London, Memoirs, 39, 1-39. doi/101144/M39.11.

Wadge, G., Costa, A., Pascal., K., Werner, C., Webb, T. (2016) The variability of refractivity in the atmospheric boundary layer of a tropical island measured by ground-based interferometric radar. *Bound. Layer Meteorol*. 161/2, 309-333. doi:10.1007/s10546-016-0168-3.

Waliser, D. E., Gautier, C. (1993) A satellite-derived climatology of the ITCZ. *J. Climate*, 6, 2162-2174

Wang, C-C., Kirshbaum., D.J. (2015) Thermally forced convection over a mountainous tropical island. *J. Atmos. Sci*., 72, 2484-2506.

Webb, T.L. (2015) High resolution atmospheric modelling of a tropical island for space geodesy. *Ph.D. thesis, University of Reading*.

Zebker H.A., Villasenor, J. (1992) Decorrelation in interferometric maps. *IEEE Trans. Geosci., Rem. Sensing,* 30/5, 950-959.

1031

Supplement 1

Method to simulate the ZWD field from GPS-derived values

In practice, we use a 4-step method to separate and interpolate the topographic and dynamic components of the zenith wet delay field before recombining them:

1. Normalize the ZWD values to sea-level equivalence for all 14 sites using the ZWD lapse rate. Assume that the remaining anomalies are due to horizontal differences in the water vapour field.

2. Interpolate the 14 (or less, depending on receiver availability) values of lateral delay to a 25 m grid using kriging to create field H.

3. Multiply the elevation values at each 25 m posting of the DEM (equivalent to field H) with the ZWD lapse rate. This gives the vertical variability due to topography, field V.

4. Add fields H (horizontal component) and V (vertical component).

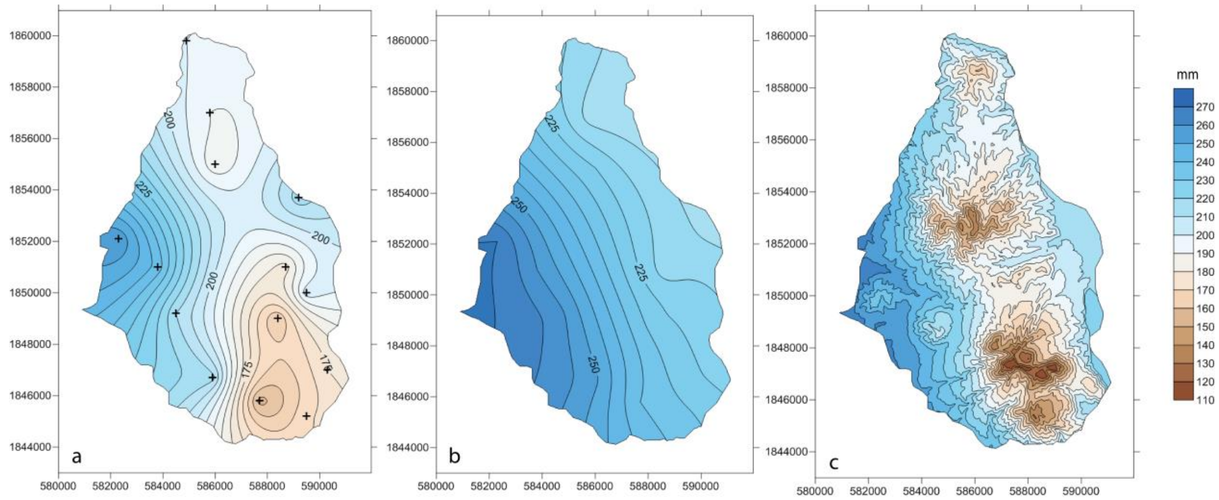

Fig. S1 ZWD fields (mm) at 17:30 (local time) on 3rd August 2013. (a) Field interpolated from the 14 GPS observation sites (black crosses). (b) Horizontal gradient field after normalising values in (a) to sea level. (c) Combined horizontal (b) and vertical fields interpolated using the water vapour lapse rate (0.14 mm/m) multiplied by the elevations of each cell of a 25 m horizontal resolution DEM.

Figure S1 shows the resulting ZWD field for the 17:30, 3rd August 2013. Low values of ZWD are concentrated along the central, mountainous, spine of the island (Fig. S1a). But the lack of observations in the central part of the island produces higher than expected values in the interpolated field. The horizontal component of the field shows a clear ENE gradient of about 50 mm of delay across the island (Fig. S1b). This gradient is the same orientation as that observed by MODIS and WMM (Fig. 4), and is of similar amplitude compared to the lee wave anomalies from WMM of ~70 mm. The full, 25m horizontal resolution ZWD field is shown in Fig. S1c.